CHAPTER 4 : DELAYED EXTRUDATE SWELL EXPERIMENTS WITH POLYMER SOLUTIONS

4.1. Introduction.

The relation between the elasticity of a material and the extrudate swell is known since the middle of the present century [1]. The phenomenon of the delayed extrudate swell, that is, the fact that with polymeric liquids the swelling starts at a distance from the exit of the die in certain regimes, is also known since about thirty years.

The first attempt to explain this phenomenon was done by Metzner et al. [2], who presented among other viscoelastic phenomena, the first photographs of the delayed die swell of a 5% polyisobutylene solution. They associated the phenomenon with stress relaxation. They considered that the relaxation time that corresponds to this phenomenon begins at λ_{te}, evaluated from the local shear rates existing as the fluid emerges from the tube, and tends toward λ_0 (the relaxation time of the fluid evaluated at conditions of zero fluid deformation) as the fluid relaxes.

Giesekus [3] presented this phenomenon with a 5% polyacrylamide solution. By combined visualization of both upstream and downstream flows, he associated the phenomenon with polymer aggregation before entering the die.

Brenchede and Klein [4] (1970) made experiments with a 6% polyisobutylene solution through dies of various length to diameter ratios (L/D). They observed a discontinuity of the flow curves at a critical shear rate, which is more accentuated the shorter the die. The extrudate presented non-homogeneous composition above this critical rate value. The delay of the extrudate swell happened far above this value. Brenchede and Klein provided a molecular explanation for the delay, which involved precipitation of the polymer.

Joseph et al. [5] presented the most systematic delayed extrudate swell experiments (1987). They examined solutions of concentrations varying from 1 to 10% and of many different polymers (polyoxyethylene, polyacrylamide, polyisobutylene and polymethyl-methacrylate). All these solutions have shown delayed swell.

The delay always occurred above a critical average extrusion velocity (u_{cr}), different for each solution. The critical quantity common to all solutions proved to be the Mach number at the exit, defined as :

$$M = \frac{2u}{c} \qquad (4.1)$$

where u is the average velocity in the die and c is the shear wave or vorticity wave speed into the fluid at rest :

$$c = \sqrt{\frac{G_c}{\rho}} \qquad (4.2)$$

where G_c is the effective rigidity or shear modulus and ρ is the density of the fluid. The delay occurs always when the Mach number is greater than 1.

Joseph [5, 8] stated that the phenomenon of the delayed die swell should be associated with a change of type in the governing equation of the vorticity :

$$\zeta(r) = -\frac{\partial u(r)}{\partial r} \qquad (4.3)$$

At the exit of the die the velocity profile is assumed to be fully developed and the vorticity is a linear function of the distance r. The vorticity decays to 0 far downstream, where the velocity profile is uniform. This relaxation of the vorticity is induced by a discontinuous prescription of the data as fluid exits, namely the absence of slip at the wall, and the absence of shear at the surface of the jet. The discontinuous prescription of the boundary values requires the readjustment of the flow from pipe flow with a linear vorticity profile at the exit, to a uniform flow profile. This readjustment is powered by waves which carry the boundary data into the jet. When the flow velocity becomes higher than the speed of these shear waves (c), the region of zero vorticity needs some time to occupy the whole diameter of the jet and that is what causes the delay.

The delayed swelling occurred as either a steady or an unsteady response to steady extrusion, depending on the fluid. In other words, the delay distance either remained constant at a constant regime, or pulsated between two extreme values. For the same polymer-solvent system steadiness or unsteadiness could depend on concentration, and the general conclusion was that the critical parameter for steadiness was the mean relaxation time, defined as :

$$\lambda = \frac{\eta_0}{G_c} \qquad (4.4)$$

with η_0 the zero shear viscosity. Solutions with relatively low relaxation times (lower than 0.1 or 0.2 s) presented steady delays and solutions with high λ unsteady delays.

Another important observation of Joseph et al. is that the phenomenon terminated at high regimes either in a large amplitude oscillation or by smoothing, with a preference for the former (even for solutions with steady delay at lower regimes). Only solutions with a very short relaxation time presented termination by smoothing. The term "smoothing" means here an important delay of the swelling, which happens in a smooth way : the delay is much higher during smoothing than at lower regimes, but it

occurs more gradually with the distance from the pipe exit. There is no abrupt increase of the section of the fluid jet, but a smooth increase.

Delvaux and Crochet [9] simulated numerically the delayed die-swell for an Oldroyd-B fluid. Their conclusions are in agreement with Joseph's theory: at Mach numbers higher than 1, the hyperbolic region of the vorticity extends downstream into the jet but does not reach the jet boundary. The change in the curvature of the jet is associated with the breakout of the hyperbolic region. The onset of the delay occurs the moment when the hyperbolic region of the vorticity reaches the boundary of the fluid. They considered the role of elastic and inertial effects in the Mach number :

$$M = \sqrt{Re\, We} \qquad (4.5a)$$

where the Weissenberg number was considered as :

$$We = \frac{\lambda u}{D} \qquad (4.5b)$$

Delvaux and Crochet concluded that the lower the Re, the higher the We for the phenomenon to be observed. However, they did not find an unquestionable value of the Mach number triggering the phenomenon.

Allain et al. [6] examined the delayed die-swell of aqueous xanthan solutions of low concentrations (500 ppm to 4000 ppm). To reduce the disturbances due to gravity and to interfacial effects they immersed the jet into a nearly buoyant miscible fluid. Their results showed that the delay happens above a critical shear rate that increases with concentration. They also observed the two different classes of behaviors: the delay was steady for the very low concentrations and unsteady for the higher ones. Also, the increase of the delay with shear rate, is faster than linear with the lower concentration solutions.

The solutions of Allain et al. have been tested by Joseph and Christodoulou [7]. Measurements of the shear wave speed of these solutions showed that, with these solutions too, the delayed die swell starts when M>1.

In the present chapter we present delayed die-swell experiments with a concentrated solution of the polyoxyethylene used also in the experiments of Chapter 2, as well as with a poly(acrylamide-acrylate) copolymer solution in a viscous solvent. The objective is to examine how the delayed swell is related to other flow characteristics (length to diameter ratio values, wall material, flow regimes and upstream instabilities). The experimental setup geometry is presented in section 4.2, and the shear viscosity of the fluids in section 4.3. Results of the PEO solution with various die lengths are given in section 4.4. In section 4.5 the influence of the die wall material

is examined and in section 4.6 the results on the copolymer solution are discussed. The conclusions are given in section 4.7.

4.2. The experimental set-up.

The experimental set-up used for the experiments of section 4.4 consisted of a large cylindrical reservoir (approximately 1 liter in volume) connected with a cylindrical tube of 20 mm in diameter and 20 cm long, and a mounting system that allows the use of dies of various lengths and diameters (Fig. 4.1). All elements were made of stainless steel. A pressurized nitrogen circuit was used to move the fluid through the dies.

All experiments were carried out at temperatures of 20+/-0.5 °C. Dies of two different diameters (0.6 and 1 mm) and various lengths (20 to 800 mm)

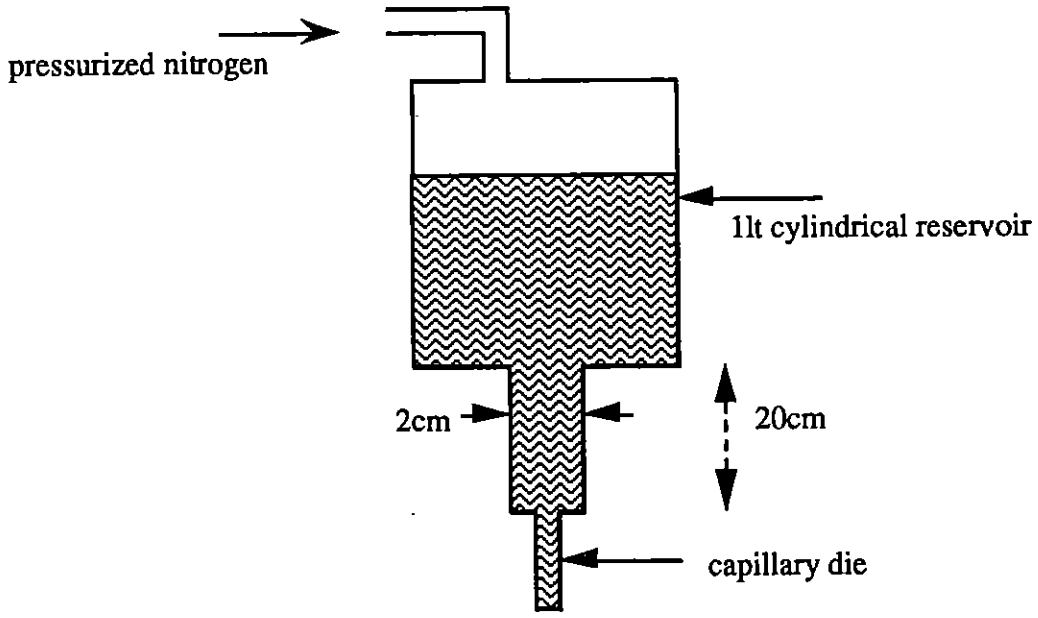

Fig. 4.1 : Schematic representation of the capillary flow experimental setup.

were used. The pressure has been controlled by precision manometers of nominal pressure ranges 0-6, 0-25 and 0-100 bars. The flow rate has been controlled by a precision balance.

The experiments described in 4.5 and 4.6 were carried out with the equipment described in Chapter 2, in which the upstream tube has the same diameter (2 cm) but is made of glass, which allows visualization of the upstream phenomena.

4.3. The shear viscosity of the solutions.

4.3.1. The PEO aqueous solution.

The results of section 4.4 refer to an aqueous PEO 4% solution. The polymer is the one referred to in Chapter 2 ($M_w=10^6$ g·mol^{-1}). Solutions of concentration of 2%, 3% and 4% have been prepared by simple mechanical agitation.

The shear viscosity of these solutions was measured with the Carrimed CSR (cone-plate geometry, cone angle: 1°, diameter: 6 cm). The results are shown in Fig. 4.2. Each measurement point was obtained at steady flow conditions. The shear viscosity of the 4% solution of the same polymer in the sugar/water syrup of Chapter 2 is reported there too, for comparison.

All three solutions proved to be highly shear-thinning. The zero shear viscosity of the 4% solution is: η_0=18.5 Pas. In the pure shear-thinning region (for $2\ s^{-1} < \dot{\gamma} < 100\ s^{-1}$) it is described very well by the equation:

$$\eta = 16.6\ \dot{\gamma}^{-0.56} \qquad (4.6)$$

which gives n= 0.44. The same slope was verified from the die measurements for $10^2\ s^{-1} < \dot{\gamma} < 10^5\ s^{-1}$ as will be demonstrated in the following.

The characteristic time proposed by Graessley and described by eq. 2.7 (section 2.3.2), has been evaluated for the three aqueous PEO solutions. They are given together with the shear viscosity characteristics in table 4.1. The non-dimensionalized viscosity curves gave a master curve for the three concentrations shown in Fig. 4.3.

The non-dimensionalized curve for the sugar/water syrup solution is shown there too, and very good agreement is noticed.

Table 4.1 : Shear viscosity data for the aqueous PEO solutions.

c (%w)	η_0 (Pa.s)	n	K (Pa.s^n)	λ (s)
2	0.8	0.54	1.83	0.0165
3	5.2	0.48	6.89	0.0713
4	18.5	0.44	16.6	0.1906

In Fig. 4.4 the variation of the zero-shear viscosity with concentration is shown for the PEO solutions, aqueous and thickened (Chapter 2). In the semi-dilute range the scaling is higher for the aqueous solutions, indicating that the sugar/syrup is a better solvent for this polymer than water.

4.3.2. The copolymer solution.

A solution of a poly(acrylamide-acrylate) copolymer (concentration of 0.5% w.) in a solvent of glucose/water (50/50 in weight) has been prepared and tested as well (the results are presented in section 4.6). The copolymer was provided by SNF FLOERGER, and its molecular weight given by the manufacturer is $14 \cdot 10^6$ g·mol^{-1}.

Shear viscosity measurements were carried out for this solution and its solvent with the same instrument and geometry as above. The solvent has a constant viscosity $\eta_s = 7.8\ 10^{-3}$ Pas. The zero shear viscosity of the solution is $\eta_0 = 30$ Pas (Fig. 4.5). For $0.3\ s^{-1} < \dot{\gamma} < 30\ s^{-1}$ its behavior is that of a power-law fluid with:

$$\eta = 7.5\ \dot{\gamma}^{-0.77} \qquad (4.7)$$

For $80\ s^{-1} < \dot{\gamma} < 210\ s^{-1}$ it shows lower shear-thinning and the viscosity is approximated by the equation:

$$\eta = 1.4\ \dot{\gamma}^{-0.35} \qquad (4.8)$$

The characteristic time λ calculated by the expression of Graessley is of 25.4 s, that is, two orders of magnitude higher than this of the PEO 4% solution in water.

4.4. Results on the 4% PEO solution.

4.4.1. The orifice flow.

Orifice flow experiments were carried out with the three aqueous semi-dilute PEO solutions, with an orifice diameter of d=0.53mm. The flow curves are shown in Fig. 4.6. For the two lowest concentrations, inertia has been important (high Reynolds numbers especially with the 2% solution), so these experiments are not directly comparable to the results of section 2. Nevertheless, scalings of similar form as the ones described in Chapter 2 with the sugar syrup solutions of the same polymer were observed.

As it was shown in Chapter 2, in the orifice flow of the entangled solutions there is an initial regime where molecular extension is limited by entanglements at low flow rates. In the present case of the aqueous 4% solution, the slope of the flow curve at low flow rates is the same as the one of the 4% thickened solution. We remind here that

these two solutions give almost identical non-dimensional shear viscosity curves (Fig. 4.3).

At intermediate regimes the slope of the flow curve increases during the build-up of the intermittent upstream instabilities. At high regimes the slope decreases again where three-dimensional instabilities become permanent. The correspondence between the flow curves of the aqueous 2, 3 and 4% solutions of the present chapter and the thickened solutions examined in Chapter 2, is better illustrated in Fig. 4.7. The flow curves are presented in the dimensionless form $C(\lambda\dot{\gamma})$: the sequence in the $C(\lambda\dot{\gamma})$ regimes for the 4% PEO in water is qualitatively similar to the one for the 4% PEO in sugar. However, the PEO-water system gives higher C values and earlier transitions to the steeper slope regime. This may be attributed to the fact that as solvent quality decreases (as indicated by shear viscosity data on Fig. 4.4 for the PEO-water system) entanglement density is decreased so molecules in a semi-dilute solution may reach higher extensions at given flow conditions.

For the PEO-water system, the values of :

$$(\lambda\dot{\gamma})_1 = 3500 \qquad (\lambda\dot{\gamma})_2 = 12000$$

characterize the end of the entanglement governed extension regime and the onset of permanent 3D unstable flow respectively.

Remark : In Fig. 4.7, the measurement points of the 4% solution correspond to the orifice flow measurements described above, as well as to a flow curve of the same solution through a short die (L=4mm, d=0.5mm). The flow curve of this later experiment is shown in Fig. 4.8.

4.4.2. The delayed swell phenomenon.

Experiments are described here with the aqueous 4% PEO solution, in order to observe the delayed extrudate swell phenomenon. This phenomenon proved to be unstable, that is, the delay was not at a constant distance at a certain regime, but it pulsated between two extremes.

The onset was difficult to observe since the phenomenon started as pulsations of the extrudate without a clear delay. These pulsations often insisted for a relatively large regime interval. Joseph et al. [5] with 1.3% and 2.5% PEO solutions observed also the unstable "version" of the phenomenon with termination at large amplitude oscillations. In our case the phenomenon terminated at high regimes at irregular oscillations between a position with a large delay and a smoothing position.

In order to show the sequence of the stages of the phenomenon, the jet of the fluid for a die of L=200mm and D=1mm is shown in Fig. 4.9. Picture 4.9(a) corresponds to a regime where no delay occurred (P=7bar). Flow was stable and high extrudate swell existed. Picture 4.9(b) corresponds to critical onset conditions : At the regime corresponding to this picture (P=9bar), pulsations occurred between this delay position and the no-delay position of the previous picture. Several pulsations per second occurred and this frequency increased with the regime.

The pictures that follow (Fig. 4.9(c), (d) and (e)), were taken at pressure levels P of 10, 12 and 15 bar respectively. A "clear" delay is shown in Fig. 4.9(c) and (d) and each picture represents an average position for the respective pressure. The magnitude of the oscillations increased also with the regime and the phenomenon terminated above 15 bar with oscillations between the position of Fig. 4.9(e) and the smoothing position explained above.

The swell ratio (swell diameter to the inner diameter of the die), does not vary essentially with the regime. It takes values in the vicinity of 3. In Fig. 4.10, with a shorter die (L=55mm, D=1mm) we notice an initial growth of the swelling (for pressures between 1 and 4 bar) before the delay starts at 6 bars. The pulsations described above are also shown here : in the same pressure we have different positions of the swell.

4.4.3. The flow curves.

The flow curves through the Φ= 0.6 mm and Φ= 1 mm dies are shown in Fig. 4.11 and 4.12 respectively. The regimes where the onset of the delayed swell was observed for each length are noted there too. In Fig. 4.12 the points of measurement that correspond to the pictures of Fig. 4.9 are also shown.

One notices at a first look that, within the experimental uncertainty of judging the initial delay onset, this onset happened at the same flow rate for all die lengths of each diameter. This first result is in agreement with the work of Joseph et al.

The flow curves presented slope changes in a log-log plot. These slope changes were, in general, more accentuated the smaller the length to the diameter ratio. The same phenomenon has been observed by Brenchede and Klein [4]. They are, as it will be shown in 4.4.6, not connected to the delayed swell phenomenon. In the smallest length die of each diameter, we notice a behavior similar to the one shown in Chapter 2 with the flow of semi-dilute PEO solutions through thin-walled orifices : A relatively slight slope in the entanglement governed molecular extension regime. A higher slope at intermediate regimes where molecular deformation causes important elastic effects. A new break of the flow curve and a smaller slope at high regimes is accompanied by

three-dimensional instabilities. In the present case of the L=20mm length dies, the slopes have been altered by viscous effects due to the capillary length. The successive slopes are 1, 1.5 and 1.

In 4.4.6 we will show that, by subtracting the pressure loss due to the entry effects, we obtain flow curves that have no slope change until the point where inertial effects become very important.

4.4.4. The flow parameters at critical conditions.

The flow parameters at critical delayed swell conditions are shown in table 4.2. u_{cr} is the mean velocity in the die, $\dot{\gamma}$ is the apparent shear rate in the die and $\dot{\gamma}_w$ is the shear rate corrected for a shear-thinning fluid:

$$\dot{\gamma}_w = \frac{3n+1}{4n}\dot{\gamma} = \frac{8(3n+1)q_v}{n\pi D^3} \qquad (4.9)$$

where n is the power-law index. Re_{gen} is the generalized Reynolds number for a shear-thinning power-law fluid [10] :

$$Re_{gen} = \frac{\rho D^n V^{2-n}}{8^{n-1} K'} \qquad (4.10)$$

where K' is the modified coefficient of the power law :

$$K' = K\left(\frac{3n+1}{4n}\right)^n \qquad (4.11)$$

Table 4.2 : Flow parameters at critical delayed swell conditions.

D (mm)	L (mm)	q_v (ml/s)	u_{cr} (m/s)	$\dot{\gamma}_w (10^3\ s^{-1})$	$\lambda\dot{\gamma}$
0.6	20	1.12	3.97	69.7	13294
0.6	55	1.08	3.83	67.2	12820
0.6	200	1.35	4.77	83.8	15971
0.6	400	1.35	4.78	83.9	15995
1	20	3.11	3.96	41.7	7950
1	55	3.26	4.15	43.8	8341
1	200	2.66	3.38	35.6	6793
1	400	3.29	4.18	44.1	8408
1	800	3.88	4.94	52.1	9930

The critical velocity is independent of the die diameter within experimental accuracy, which seems to reinforce the criterion based on the Mach number defined by eq. (4.1). There seems to be a trend of the velocity to increase with the length to diameter ratio (L/D) for L/D < 50. But the variation is limited to 10% in the total (L/D) range for the D=0.6mm dies and 18% for the D=1mm dies. By comparing these variations with the measurement error, no unquestionable conclusions can be drawn.

The onset of the delayed swell occurs at regimes between the onset of the elastic effects and the onset of permanent knitting instabilities. It has been shown in Chapter 2 that the value of the parameter $\lambda\dot{\gamma}$ which corresponded to the onset of these instabilities is a function of concentration. For the concentration of 4%, the critical $(\lambda\dot{\gamma})_2$ was 15400. The onset of the delayed swell is, thus, very close to the onset of the three-dimensional instabilities.

4.4.5. The viscosity curve.

The apparent viscosity curves $\eta_{ap}(\dot{\gamma}_{ap})$ are shown in Fig. 4.13 and 4.14. One can see there the end effect [13] : There is a departure from power-law behavior which decreases as the die length increases.

The so-called Bagley correction was applied to the measurements : the pressure loss was plotted as function of the shear rate and of the length-diameter ratio (Fig. 4.15 and 4.16). The measurement points found in these figures correspond to the dies of all lengths and both diameters, as well as to the combined flow curves of the orifice flow described in 4.4.1, and the flow though a short capillary shown already in Fig. 4.8 and described more in detail in 4.5.2. These values of the pressure loss $P(\dot{\gamma})$ have been considered in the following as the losses corresponding to the entry effects : P_e.

Using data from two orifice diameters on the same Bagley plot may be justified by the following analysis. The total pressure is :

$$P_t = P_e + P_c \qquad (4.12)$$

P_c is the pressure drop due to viscometric flow in the capillary and is given by :

$$P_c = \frac{4L}{D}\tau_w \qquad (4.13a)$$

where τ_w is the wall shear stress. In the absence of slip :

$$\tau_w = \eta(\dot{\gamma}_w)\,\dot{\gamma}_w \qquad (4.13b)$$

with $\dot{\gamma}_w$ the wall shear rate . For a power-law fluid, the Rabinowitz correction gives :

$$\dot{\gamma}_w = \frac{3n+1}{4n}\frac{32\,q_v}{\pi D^3} \qquad (4.13c)$$

P_e is the excess pressure drop in the entry flow. As shown in chapter 2, $P_e = A\,\dot{\gamma}^B$, where A and B depend on fluid properties but not on contraction ratio, provided that contraction ratio is large. Also $\dot{\gamma}$ was defined by the same relation as (4.13c). Equation (4.12) is thus written as :

$$P_t = P_e(\dot{\gamma}_w) + \frac{4L}{D}\eta(\dot{\gamma}_w)\,\dot{\gamma}_w \qquad (4.13d)$$

According to (4.13d) extrapolation of the $P_t\left(\frac{L}{D}\right)$ relation to L/D = 0 for a given $\dot{\gamma}_w$ gives the value of P_e at $\dot{\gamma}_w$.

Having determined P_e from the Bagley plot, τ_w is determined from (4.13a), and the shear viscosity is derived by :

$$\eta = \frac{\tau_w}{\dot{\gamma}} \qquad (4.14)$$

In eq. (4.14) the correction of Rabinowitsch was taken into account for the shear rate.

The resulting viscosity agrees very well with the rotative geometry measurements, and continues to much higher shear rates with the same slope (Fig. 4.17).

4.4.6. The influence of the entry loss on the flow curves.

We examined the importance of the entry losses for the total pressure loss. The plot of the P_t and the P_c as functions of the corrected shear rate $\dot{\gamma}$ are shown in Fig. 4.18 and 4.19. Filled symbols correspond to the total pressure drop P_t whereas empty symbols correspond to the pressure drop into the capillary $P_c = P_t - P_e$.

The straight lines that correspond to the slope n=0.44 are shown there too. It is clear in Fig. 4.18 and 4.19 that for the longest dies ($L \geq 55$mm for both diameters), the slope change observed when the total loss is plotted, is removed when plotting $P_c(\dot{\gamma})$. That is, by removing the entry losses, and, by consequence the elastic effects, we remain with the viscous effects due to the flow into the capillary. This is valid for

$\dot{\gamma} < 1.15\ 10^5\ s^{-1}$ for the D=0.6mm and for $\dot{\gamma} < 5\ 10^4\ s^{-1}$ for the D=1mm dies. At these shear rate values, inertial effects become very important (Re_{gen} = 200). Thus, pressure increases rapidly with shear rate for higher regimes. Moan et al. [13] have observed that strong inertial effects start at about Re=600 for profiled entry capillary and earlier (Re=300) for 180° entry capillary.

4.4.7. Slip at the wall.

To examine the possibility of slip at the wall for the flow of the PEO solution through the capillaries, the apparent shear rate was plotted as a function of the shear stress at the wall for the longest capillary of each diameter. In the case of a slip velocity Us, and when the ratio L/R approaches infinity, it is [12] :

$$\frac{3n+1}{n}\ U_s = \left(\frac{d\dot{\gamma}_{ap}}{d\left(\frac{1}{R}\right)}\right)_{\tau_{ap}} \qquad (4.15)$$

In the present case no significant difference was detected between the $\dot{\gamma}_{ap}$ of each diameter at a fixed shear rate (Fig. 4.20). So slip does not seem to occur.

4.5. The influence of the wall material on the phenomenon.

In order to investigate the influence of the wall material, experiments were conducted with two dies of different materials.

4.5.1. The two dies.

The geometries of the two dies were identical: L= 4 mm, D= 0.52+/-0.02 mm. The first die was made of stainless steel and the second one of PTFE. They have both been fabricated by drilling a hole in cylinders of thickness L=4mm of the corresponding material, and they were mounted on the experimental setup described in Chapter 2 (free jet configuration), in order to observe the upstream flow simultaneously.

4.5.2. The flow curve.

The 4% PEO solution was used as experimental fluid here too. The flow curve in the steel die has already been discussed in section 4.4.1. The flow curves showed a change in their slope (Fig. 4.21). The flow rates for a given pressure were identical in the two dies below this slope change. At higher regimes the flow rate is higher for the PTFE die by about 10%. The increase in flow rate may indicate macroscopic slip at the wall of the capillary.

The slope change was due to the onset of permanent knitting as will be discussed in the following. It occurred at V=5m/s and the corresponding shear rate is $\dot{\gamma} = 1.05\ 10^5\ s^{-1}$.

4.5.3. Instabilities and delayed swell.

For pressures along the elastic regime (P<7bar), intermittent knitting instabilities were observed upstream in the vicinity of the orifice. The same kind of intermittent instabilities was also observed for the PEO solutions in a thick solvent for this concentration range in the intermediate flow regime. These instabilities were transferred downstream to the fluid jet. A connection was obvious between the frequency of the upstream instabilities and the pulsations of the jet. These pulsations resulted in a movement of helicoidal form of the jet. This phenomenon was obvious in the jet near the die exit. As the liquid is relatively mobile, gravity pulled the extrudate and the helicoidal form of the jet did not persist at distances higher than 1-2 cm from the die exit.

In the second part of the curve, at regimes higher than the slope change, the upstream instabilities became permanent and were obvious at a very big region of the upstream tube. As the velocity there became much higher, the helicoidal movement of the jet was observable in a much higher downstream length.

The delay of swell has been perceptible in its unstable form described previously, at P= 6bar, and it has been superimposed to the melt fracture type instabilities. It has been unstable at all regimes and the maximal delay distance increased with the regime. It terminated by oscillations between delay and smoothing, at P= 13bar. At all regimes it coexisted with the instabilities previously described.

All the above mentioned phenomena occurred at both steel and PTFE dies. The only difference observed was that swelling was in about 20 - 30% higher with the PTFE die.

The general conclusion taken out of the present experiment, as well as with an experiment with a more viscous solution described in 4.6, which were carried out in

order to observe the upstream flow in delayed swell conditions, is that, the delayed swell phenomenon occurs at a regime where elastic effects dominate the upstream flow. Its onset is very close to the flow parameters characterizing the appearance of 3D unstable flow upstream of the contraction.

4.5.4. Degradation of the solution.

A degradation of the solution has been observed as far as its shear viscosity is concerned. At Fig. 4.22 the viscosity of the solution is shown, after one and two passages though the L=20mm, D=0.6mm die at shear gradients of the order of 10^5 s^{-1}. We notice that the Newtonian plateau value is divided by a factor of the order of 2, after each passage, whereas for high shear gradients it remains the same. To avoid the influence of the degradation, a new sample of the solution has been produced and used for each capillary die.

4.6. Experiment with the acrylamide-acrylate copolymer solution.

The flow curve of the 0.5% acrylamide-acrylate copolymer solution through the steel die of section 4.5 (L=4mm, d=0.5mm), is shown in Fig. 4.21. The slope of the flow curve before the slope change was 1.2. A much slighter slope existed at permanently unstable regimes (0.5).

The phenomena observed during the flow of this solution were identical with those described in detail in section 4.5.3 for the PEO 4% solution. The same stages of intermittent and permanent knitting have been followed here too and the delayed swell has been superimposed to them too. Though the formation of huge helicoidal drops hindered observation, the delayed swell phenomenon seemed to exist at all flow rates examined.

The onset of instabilities occurred at $\dot{\gamma} = 7.2\ 10^3\ s^{-1}$ and as $\lambda = 25.4s$ it is $\lambda\dot{\gamma} = 182\ 10^3$.

4.7. Conclusions.

The delayed die-swell is a phenomenon believed to result from shear wave propagation associated with a change in the boundary conditions as the fluid exits from the capillary.

Previous work by Joseph and coworkers showed that, if this is the case, the onset of delayed die swell should occur at a critical velocity, independent of the capillary dimensions.

Experiments with an aqueous semi-dilute PEO solution were performed at various values of the (L/D) ratio, including orifice flow ($L \cong 0$). For the latter, the results of chapter 2 concerning flow regimes were confirmed.

Delayed swell was observed above a certain flow rate for all capillary geometries tested. Exact determination of the onset conditions was difficult in some cases due to instabilities along the extrudate. Our results show that when $L/D > 50$, a critical velocity independent of capillary dimensions characterizes its onset, in agreement with observations of Joseph et al. For $L/D < 50$, the onset velocity seems to increase with L/D.

The onset of the delayed swell does not affect the evolution of P_g with q_v. P_g here is the total pressure loss that is, viscous pressure loss in the capillary and entry effects in the converging flow upstream of the capillary. Entry effects were evaluated by the Bagley method. The corresponding flow curve was very close to the one obtained in orifice flow. It was shown that changes of slope in the P_g - q_v curves is due to changes of slope associated with the flow regimes studied in chapter 2.

Further aspects of the delayed swell phenomenon were examined :

The onset of the delayed swell occurs during the intermediate regime where elastic effects are dominant due to considerable molecular extension. As shown in chapter 2 and confirmed here, the upstream flow is characterized by intermittent 3D instabilities. At higher flow rates, the upstream flow is permanently unstable.

The onset of the delayed swell occurs at a value of $\dot{\gamma}$ smaller but close to the fully unstable regime. As L/D decreases, the difference between these two characteristic $\dot{\gamma}$ values diminishes. For $L/D = 8$, onset of delayed swell and unstable flow occur simultaneously.

Results obtained with a PTFE die for $L/D = 8$ seem to indicate that slip may accompany the onset of the delayed swell. The effect of wall material for different L/D values needs to be further examined.

References.

1. A. C. Merrington, "Flow of viscoelastic materials in capillaries", Nature, 152 (1943) 663.
2. A. B. Metzner, J. L. White and M. M. Denn, "Behavior of viscoelastic materials in short-time processes", Chem. Eng. Prog., 62 (1966) 81-92.
3. H. Giesekus, "Verschiedene phaenomene in stroemungen viscoelastischer fluessigkeiten durch duessen", Rheologica Acta, 8 (1969) 411-421.
4. E. Brenchede and J. Klein, "Druckverluste und instabiles Fliessen elastischer Flussigkeiten im Hochdruck-Kapillarviskosimeter", Rheologica Acta, 9 (1970) 130-136.
5. D. D. Joseph, J. E. Matta and K. Chen, "Delayed die swell", J. Non Newt. Fluid Mech., 24 (1987) 31-65.
6. C. Allain, M. Cloitre, P. Perrot and D. Quemada, "Die swell in semi-rigid polymer solutions", Eur. J. Mech. Fluids, 12 (1993) 175-186.
7. D. D. Joseph and C. Christodoulou, "Independent confirmation that delayed die swell is a hyperbolic transition", J. Non Newt. Fluid Mech., 48 (1993) 225-235.
8. D. D. Joseph, "Fluid Dynamics of Viscoelastic liquids", Springer Verlag, New York, 1990.
9. V. Delvaux and M. J. Crochet, "Numerical simulation of delayed die swell", Rheologica Acta, 29 (1990) 1-10.
10. D.V. Boger, "Viscoelastic flows through contractions", Ann. Rev. Fluid Mech., 19 (1987) 157-182.
11. J.M. Piau, N. El Kissi and B. Tremblay, "Low Reynolds number flow visualization of linear and branched silicones upstream of orifice dies", J. Non Newt. Fluid Mech., 30 (1988) 197-232.
12. J.M. Piau, N. El Kissi and B. Tremblay, "Influence of upstream instabilities and wall slip on melt-fracture and sharkskin phenomena during silicone extrusion through orifice dies", J. Non Newt. Fluid Mech., 34 (1990) 145-180.
13. M. Moan, G. Chauveteau and S. Ghoniem, "Entrance effect in capillary flow of dilute and semi-dilute polymer solutions", J. Non Newt. Fluid Mech., 5 (1979) 463-474.

TABLES AND FIGURES

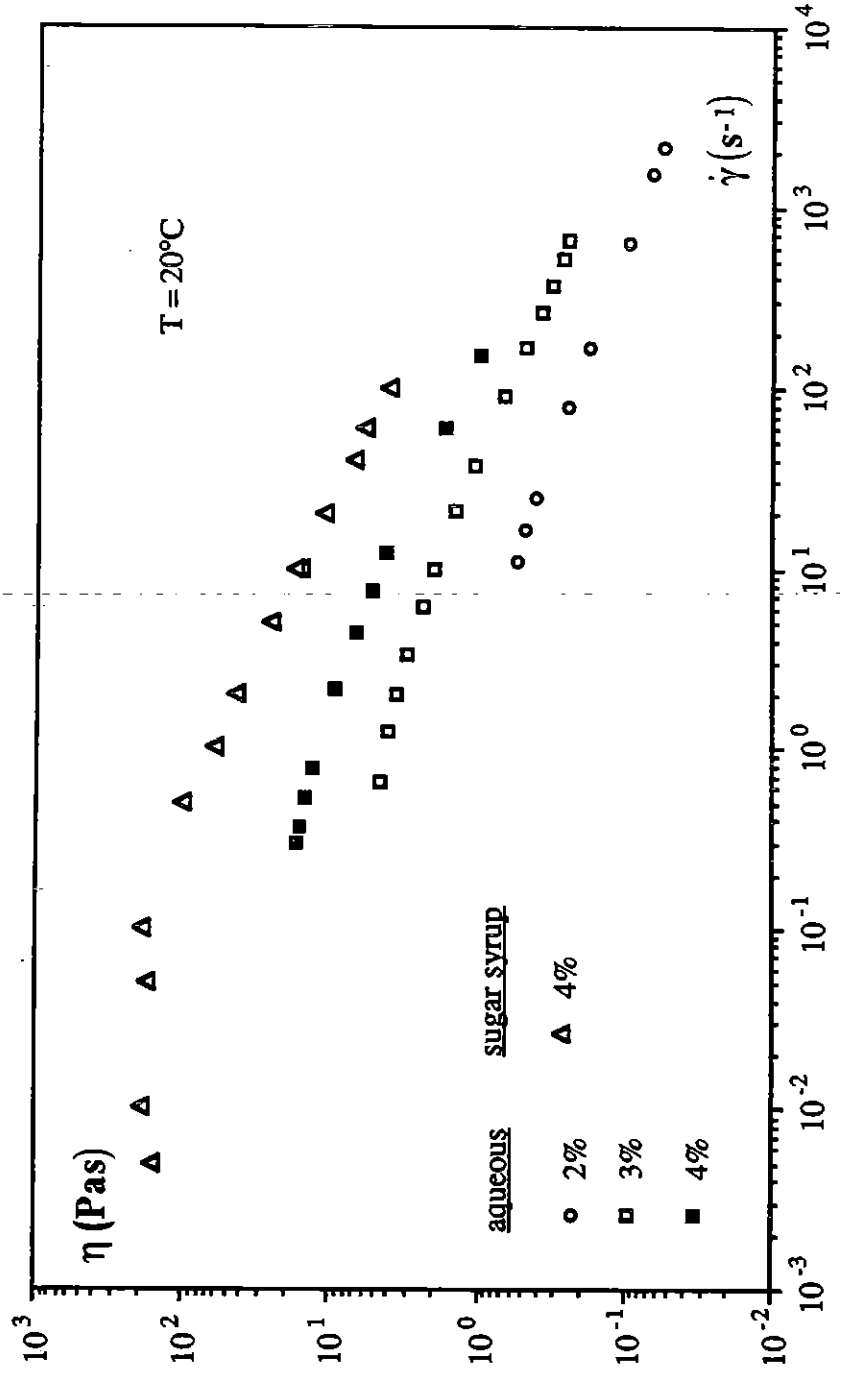

Figure 4.2 : Shear viscosity of the three concentrated aqueous solutions.

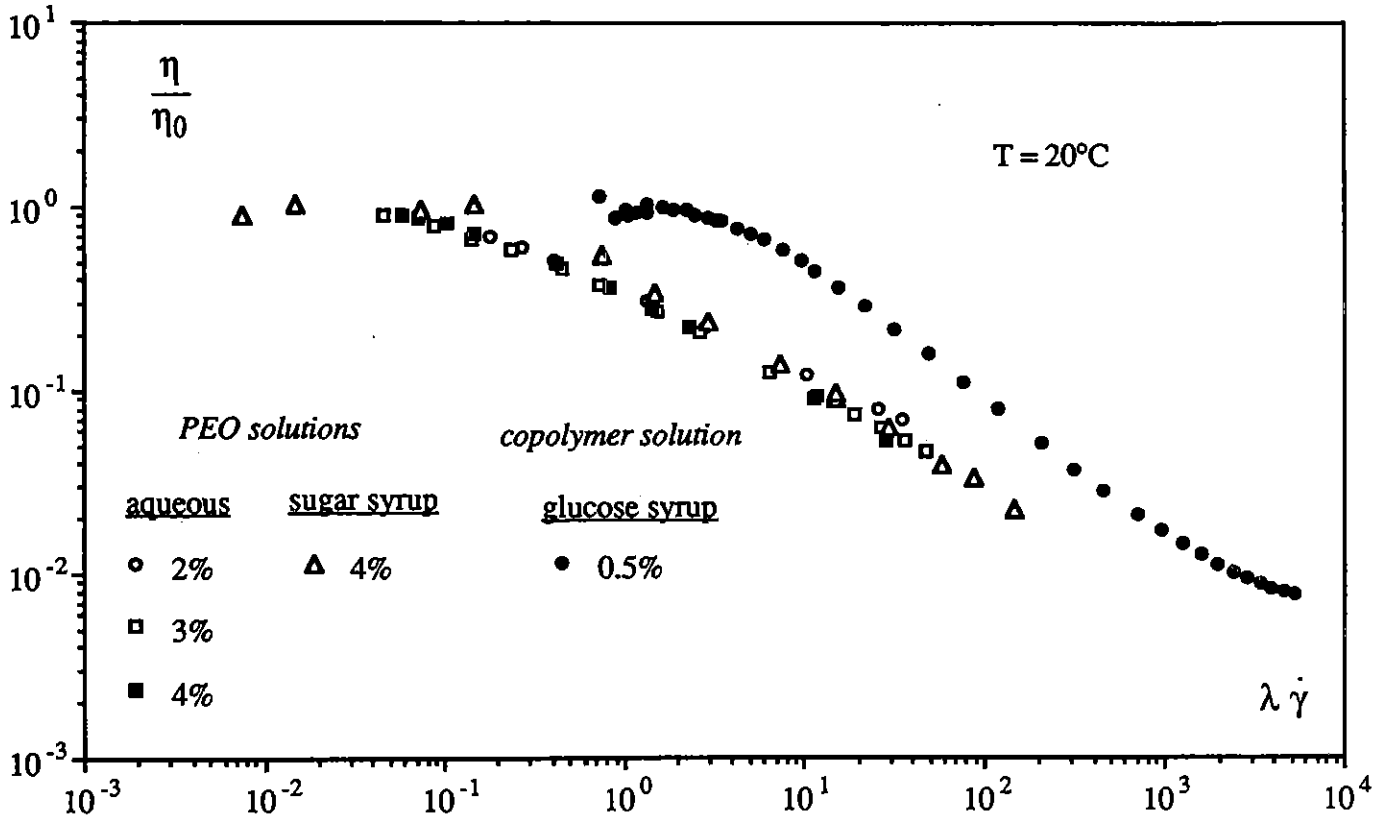

Figure 4.3 : Master curve of the relative viscosity of the aqueous PEO solutions.

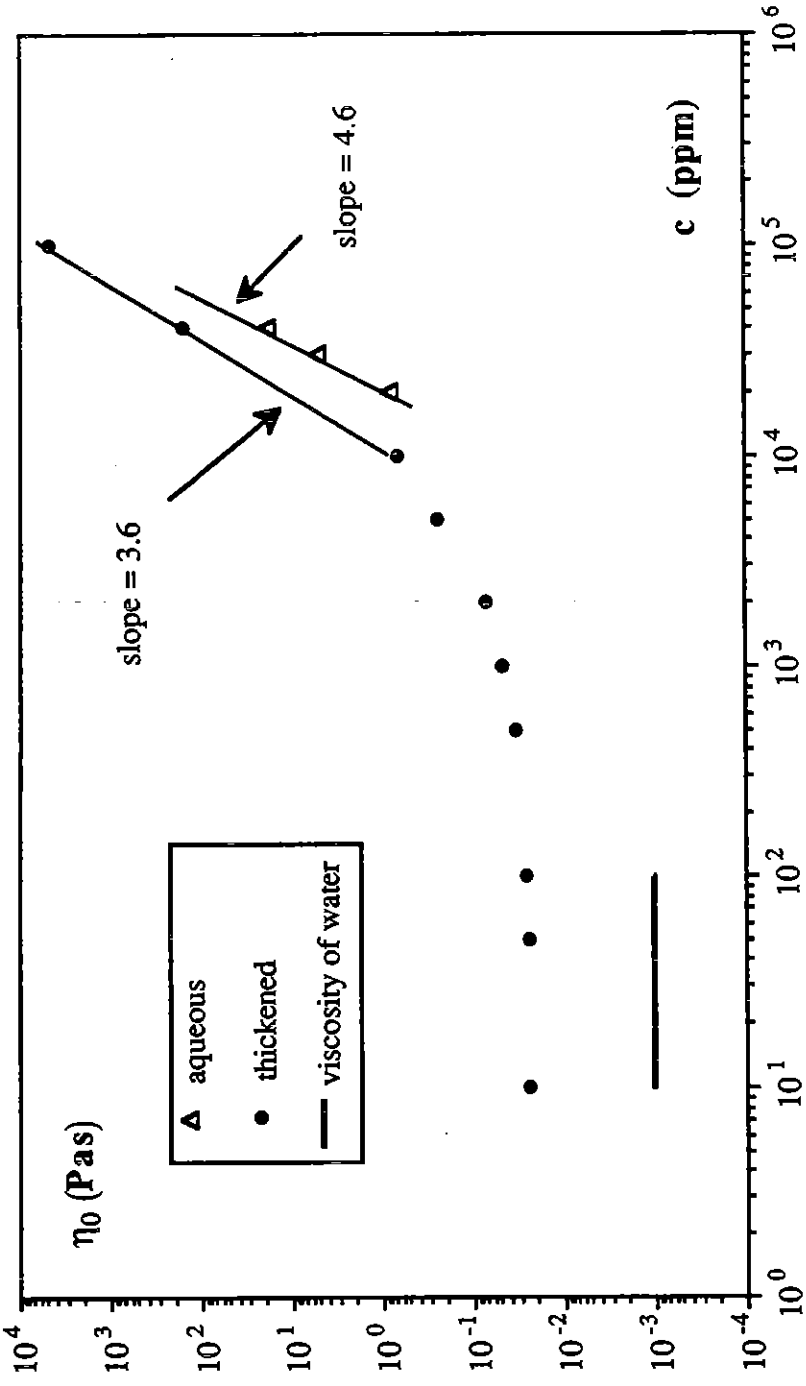

Figure 4.4 : Zero shear viscosity versus concentration for the PEO solutions : aqueous and thickened

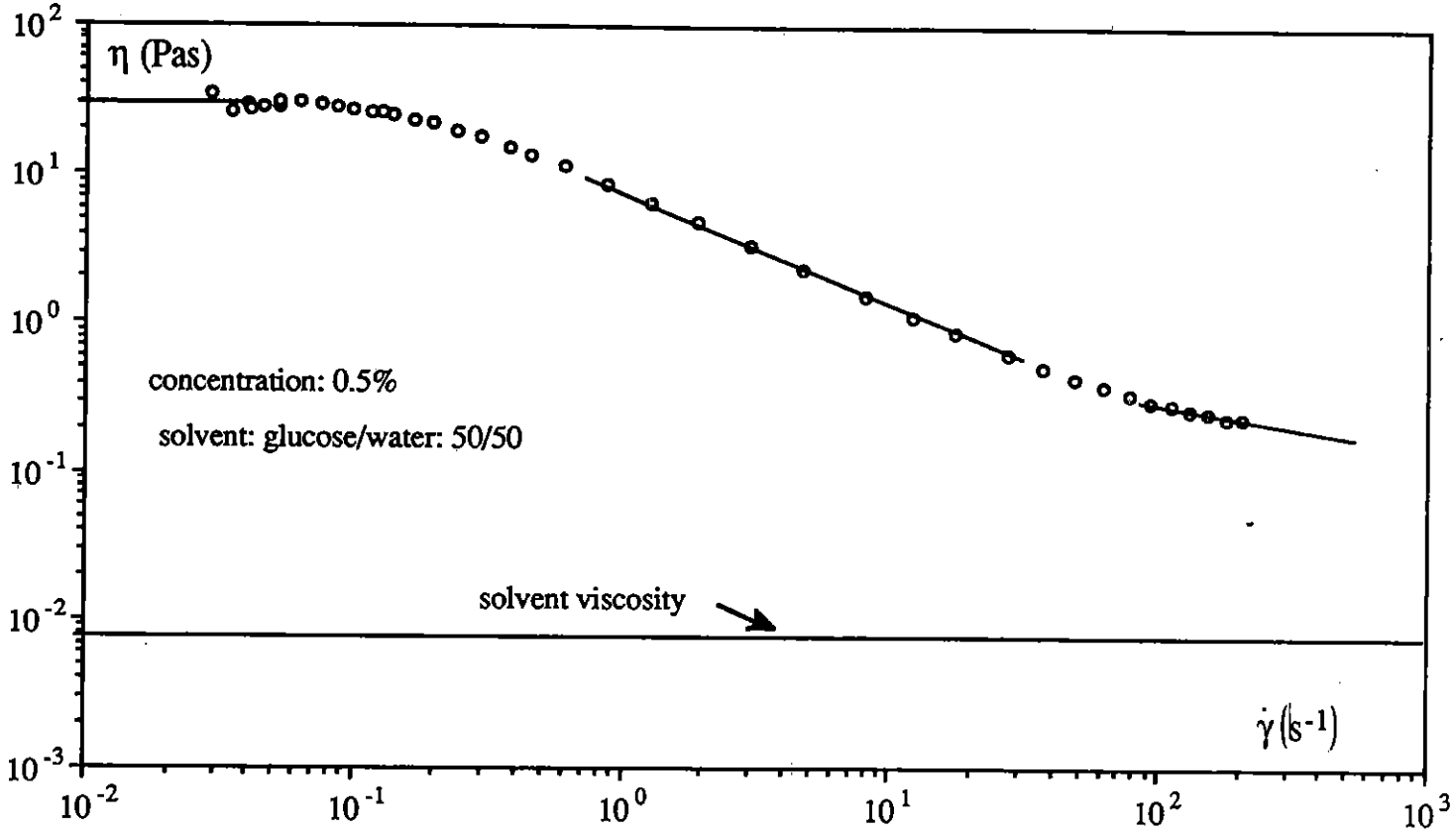

Figure 4.5 : Shear viscosity of the 0.5% solution of the copolymer

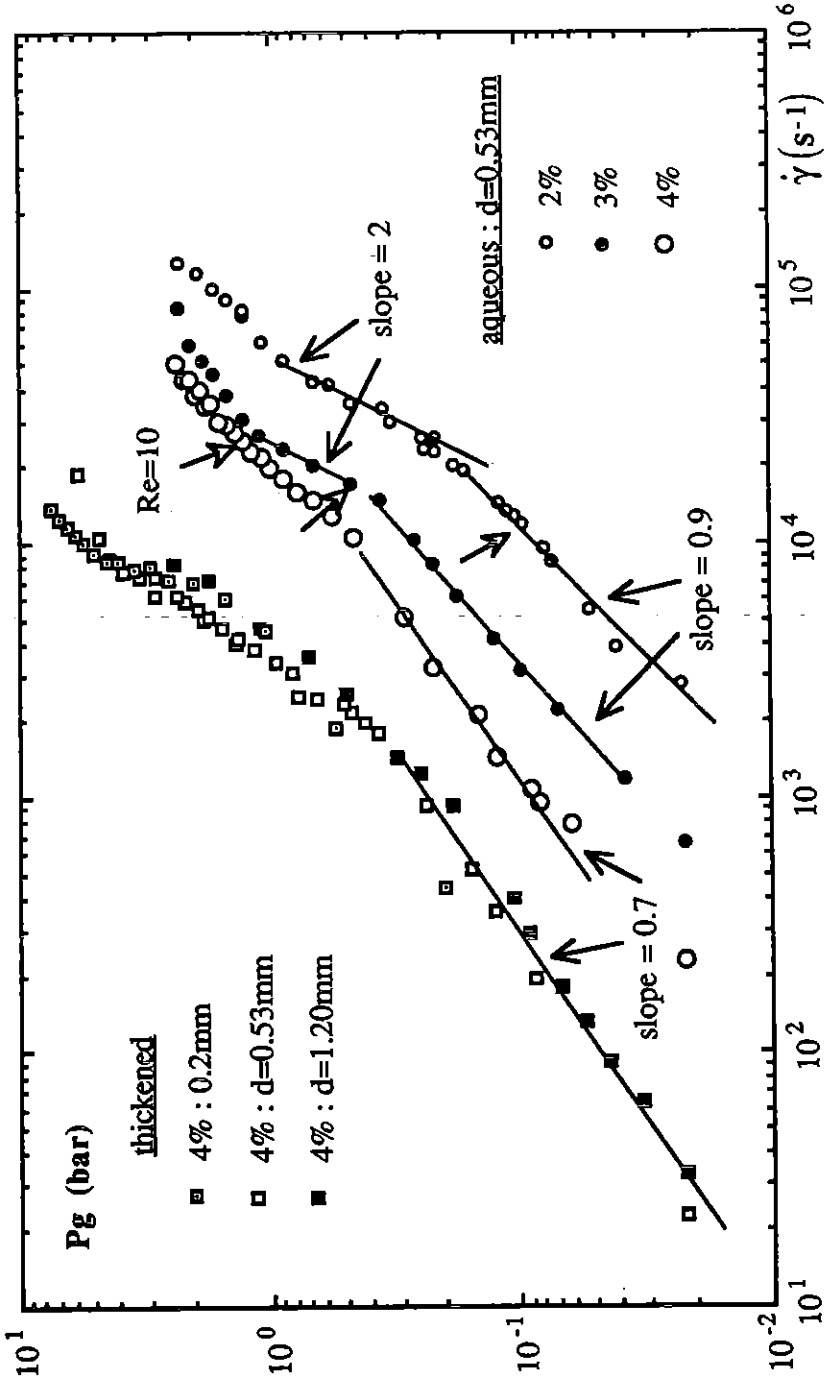

Figure 4.6 : Flow curves of PEO solutions : Aqueous and thickened.

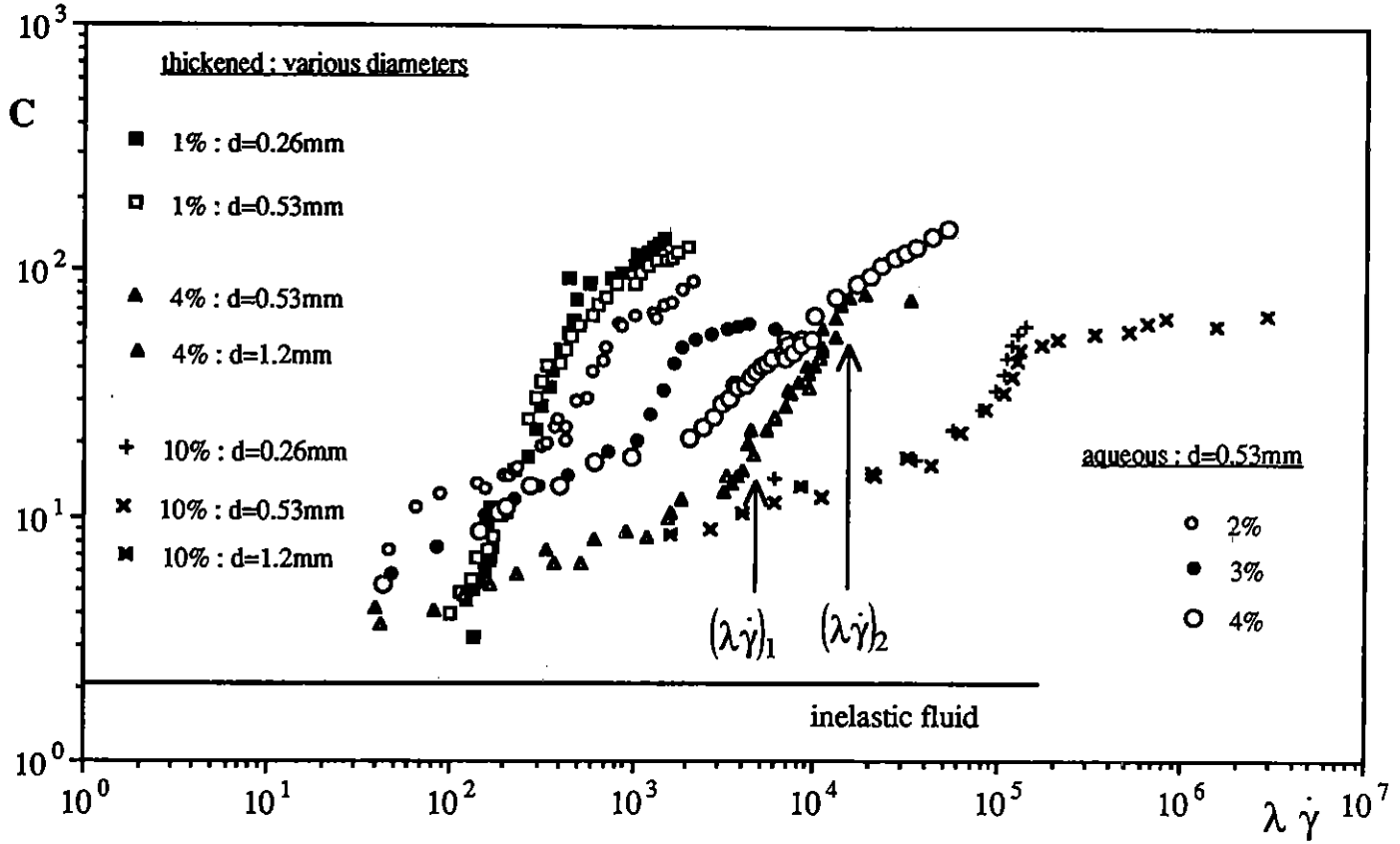

Figure 4.7 : C coefficient versus Weissenberg number for the PEO solutions. Aqueous and thickened.

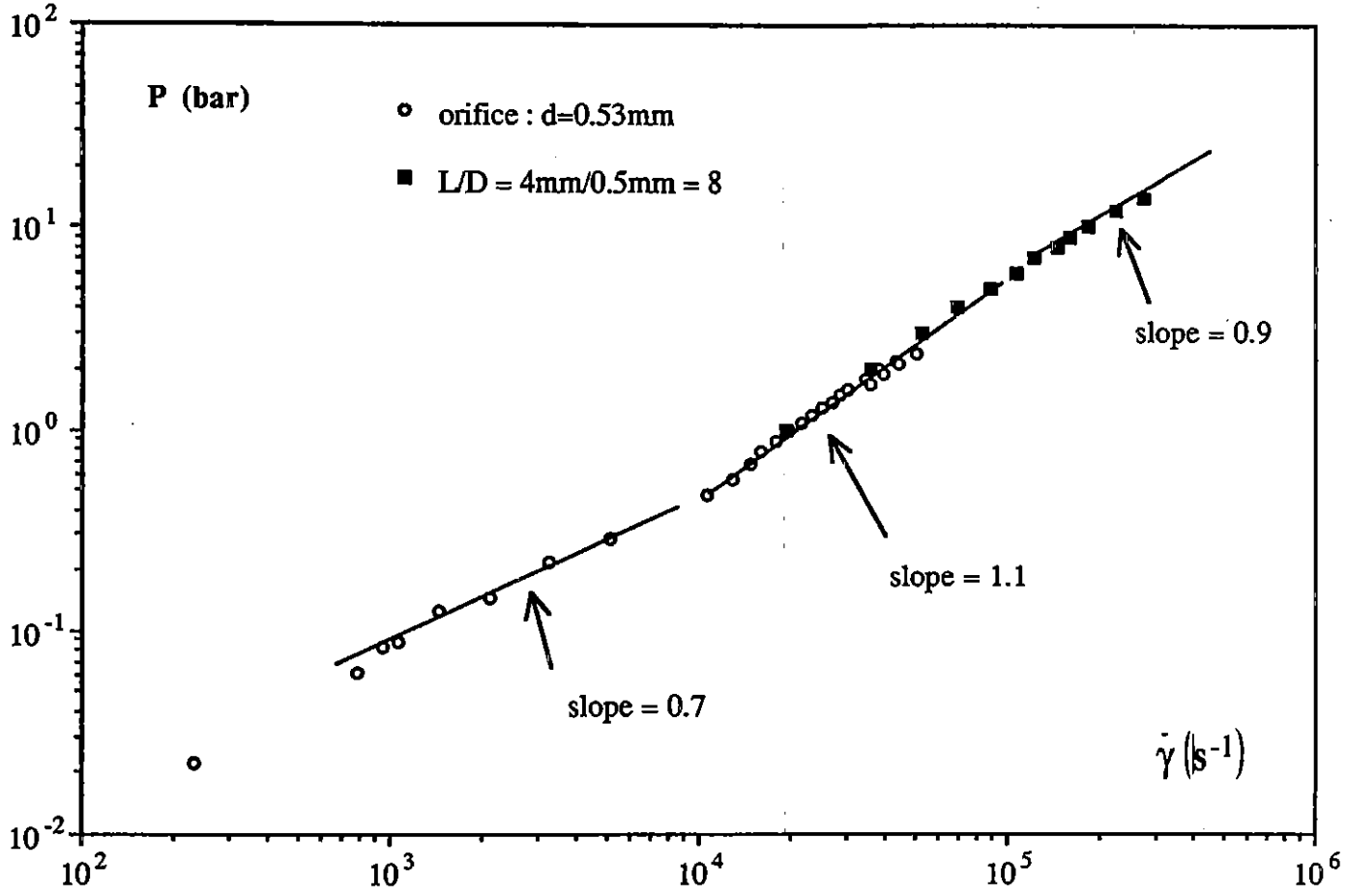

Figure 4.8 : Comparison of two flow curves of the aqueous 4% PEO solution :
An orifice die (d=0.53mm) and a capillary die (L=4mm, d=0.5m)

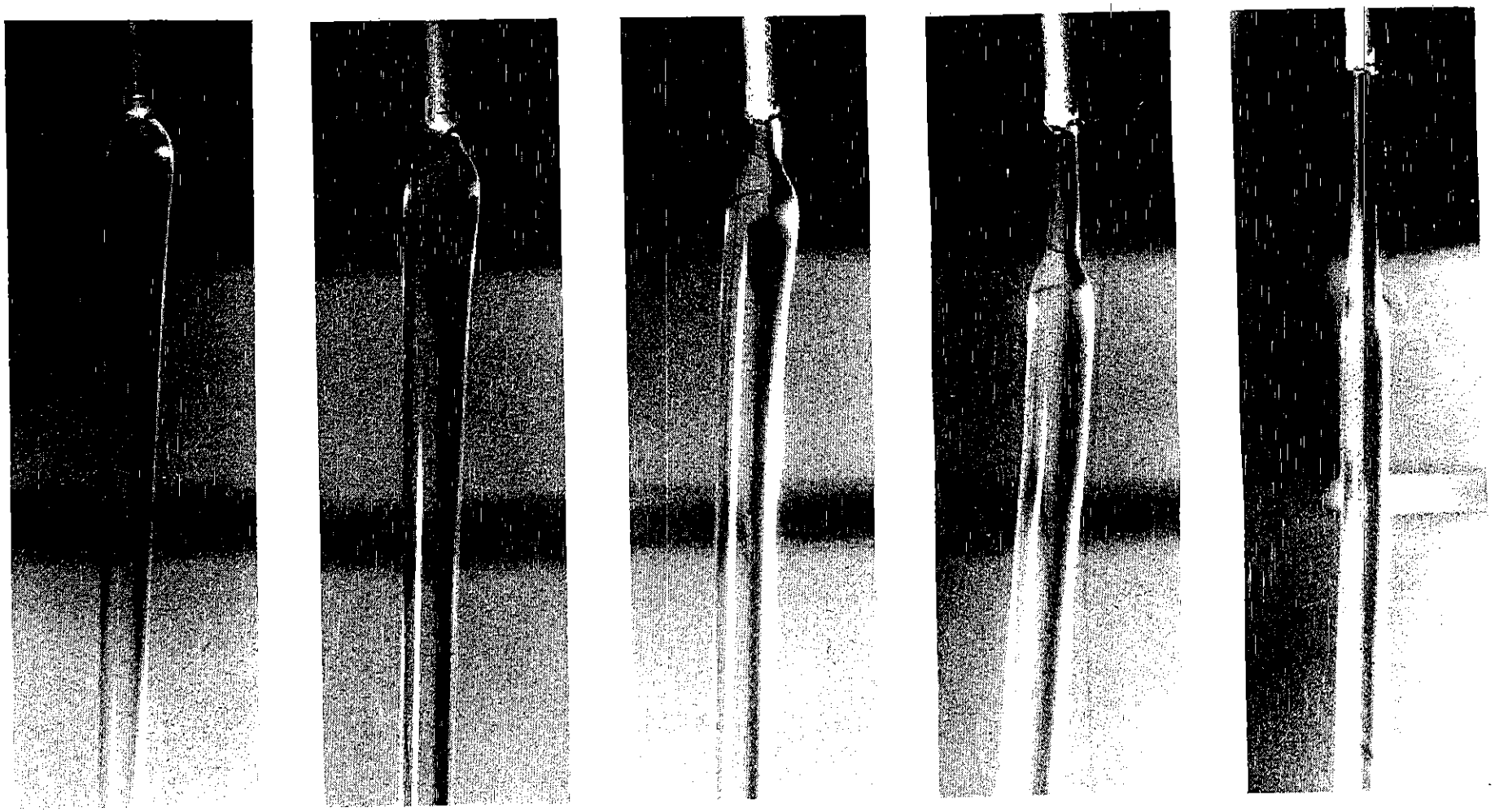

(a) Pt= 7bar, qv=1.60ml/s (b) Pt= 9bar, qv=2.45ml/s (c) Pt=10bar, qv=3.00ml/s (d) Pt=12bar, qv=3.80ml/s (e) Pt=15bar, qv=4.80ml/s

Figure 4.9 : Visualization of the fluid jet. L=200mm, D=1mm.

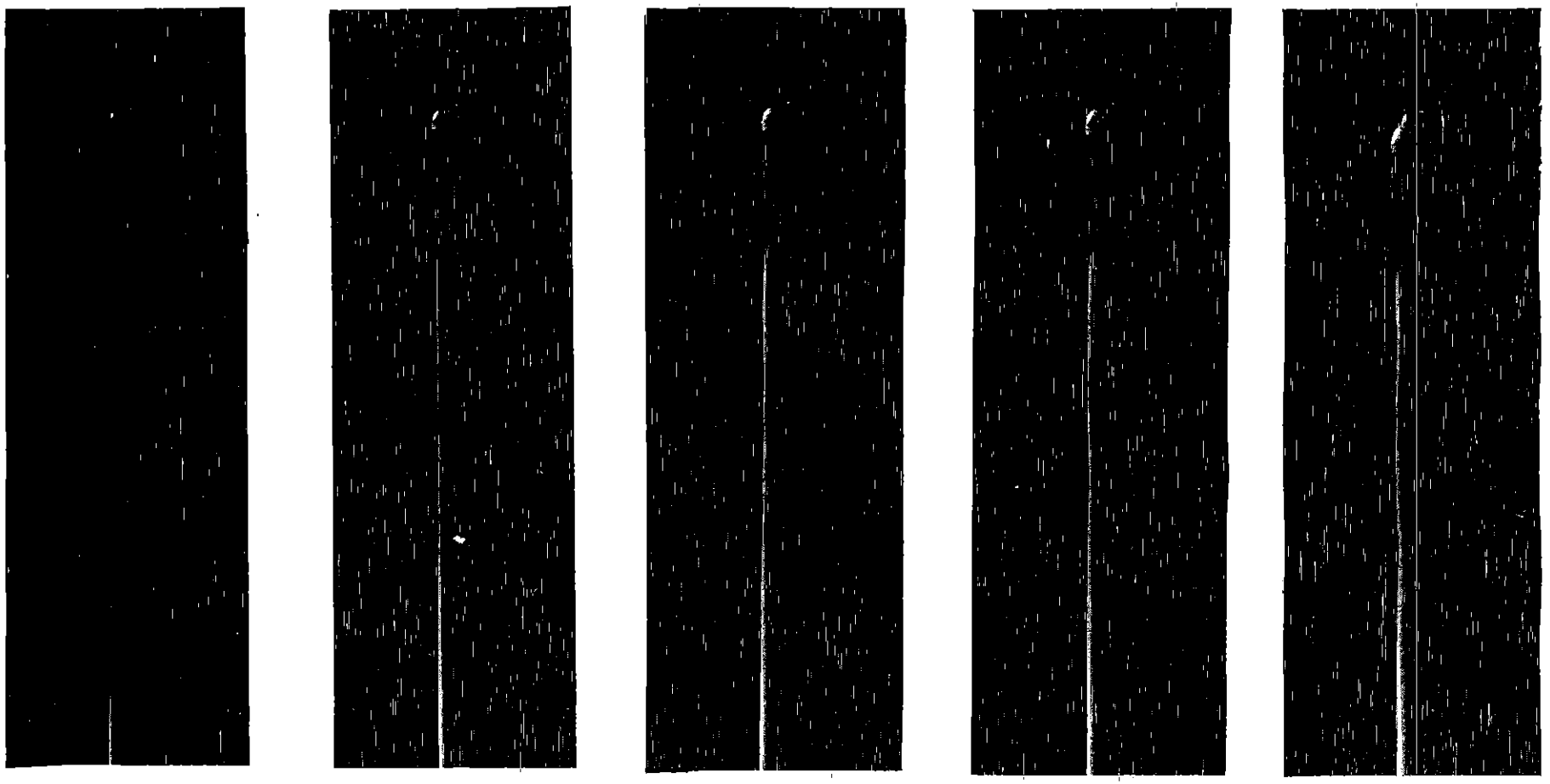

(a) Pt=1bar, qv=0.55ml/s (b) Pt=2bar, qv=1.29ml/s (c) Pt=3bar, qv=2.12ml/s (d) Pt=4bar, qv=2.57ml/s (e) Pt=6bar, qv=3.79ml/s

Figure 4.10 : Visualization of the fluid jet. L=55mm, D=1mm.

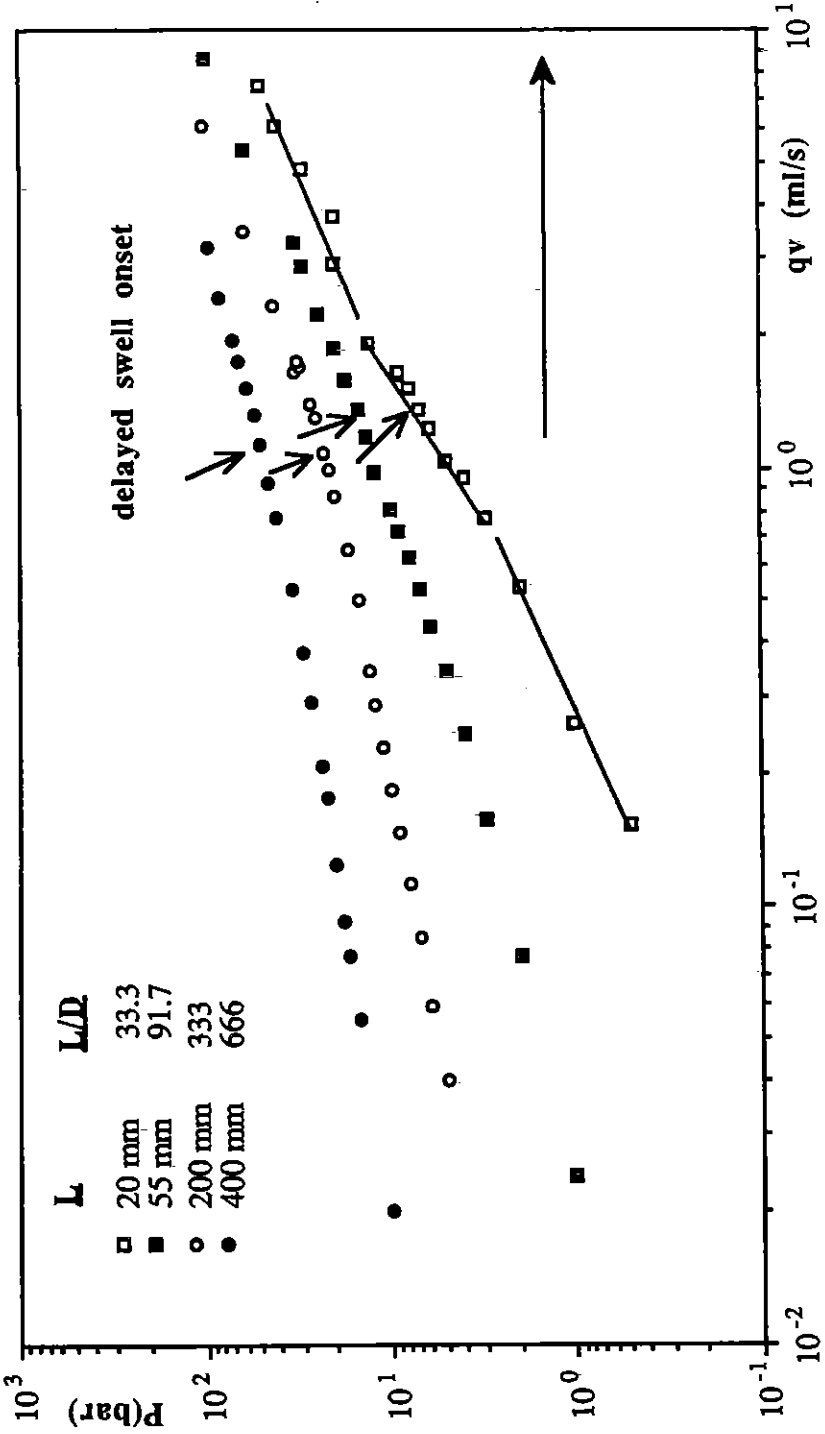

Figure 4.11 : Flow curves of the PEO 4% solution through dies of 0.6 mm.

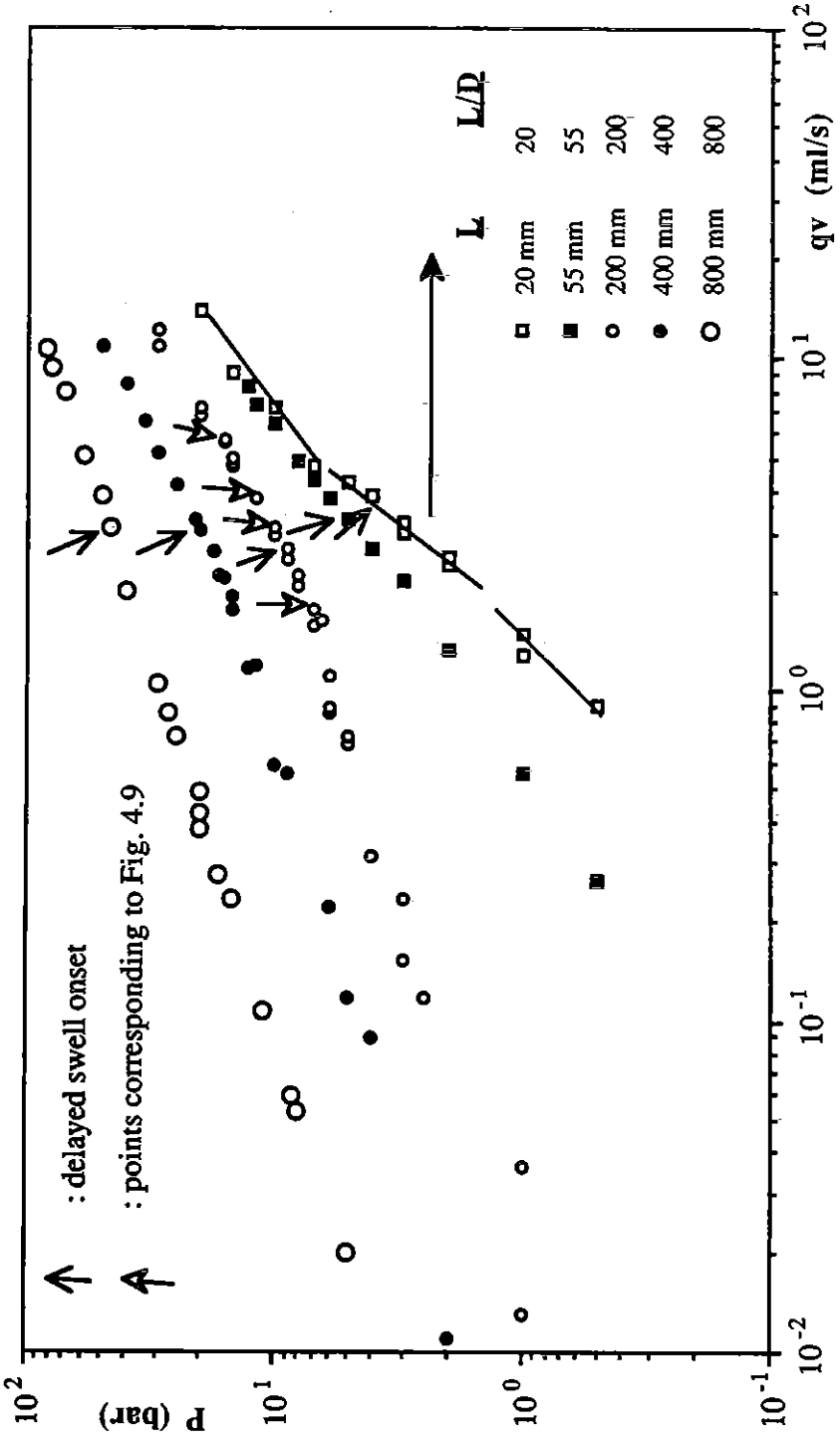

Figure 4.12 : Flow curves of the PEO 4% solution through dies of 1 mm.

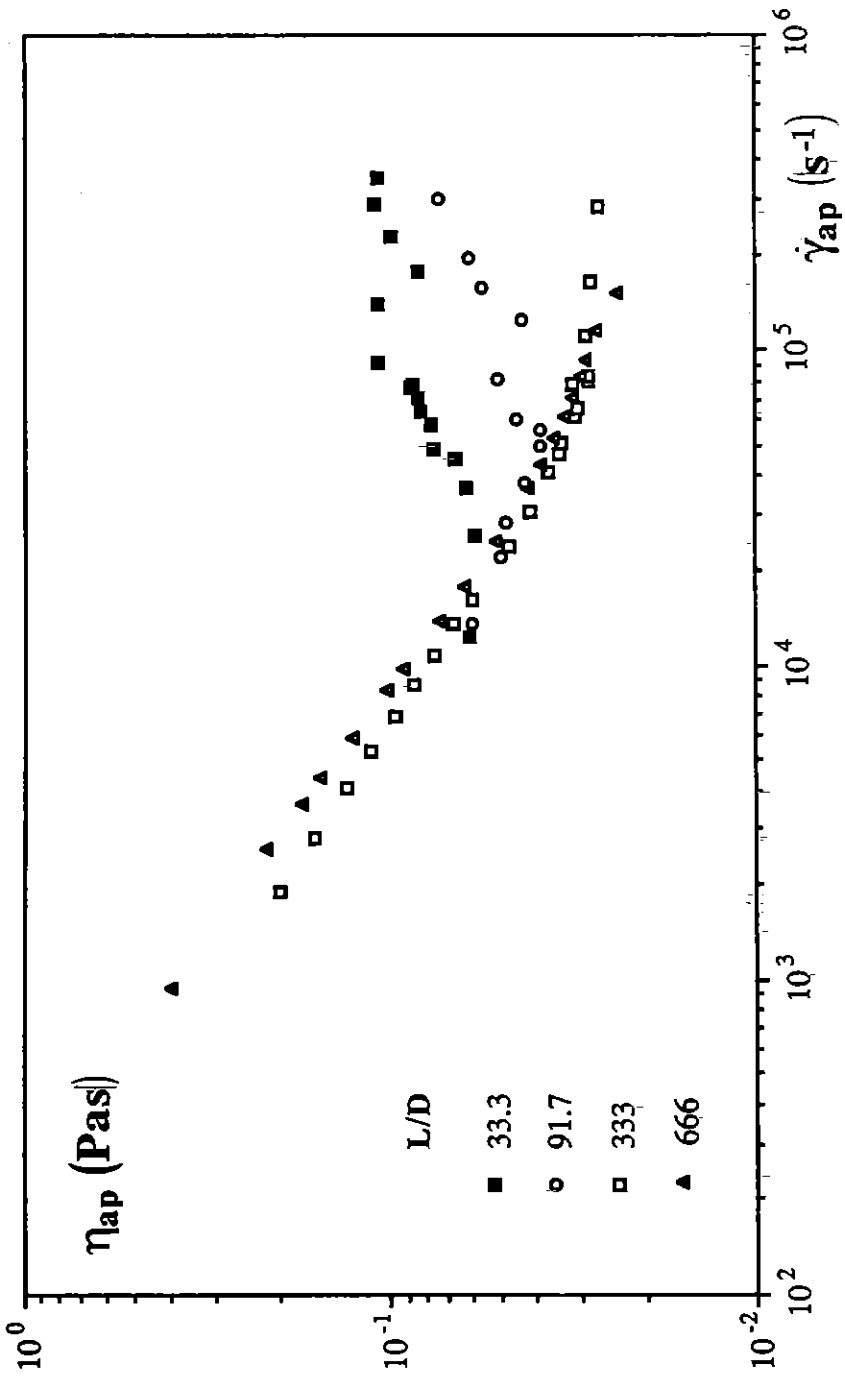

Figure 4.13 : End effect for the dies of diameter D=0.6 mm.

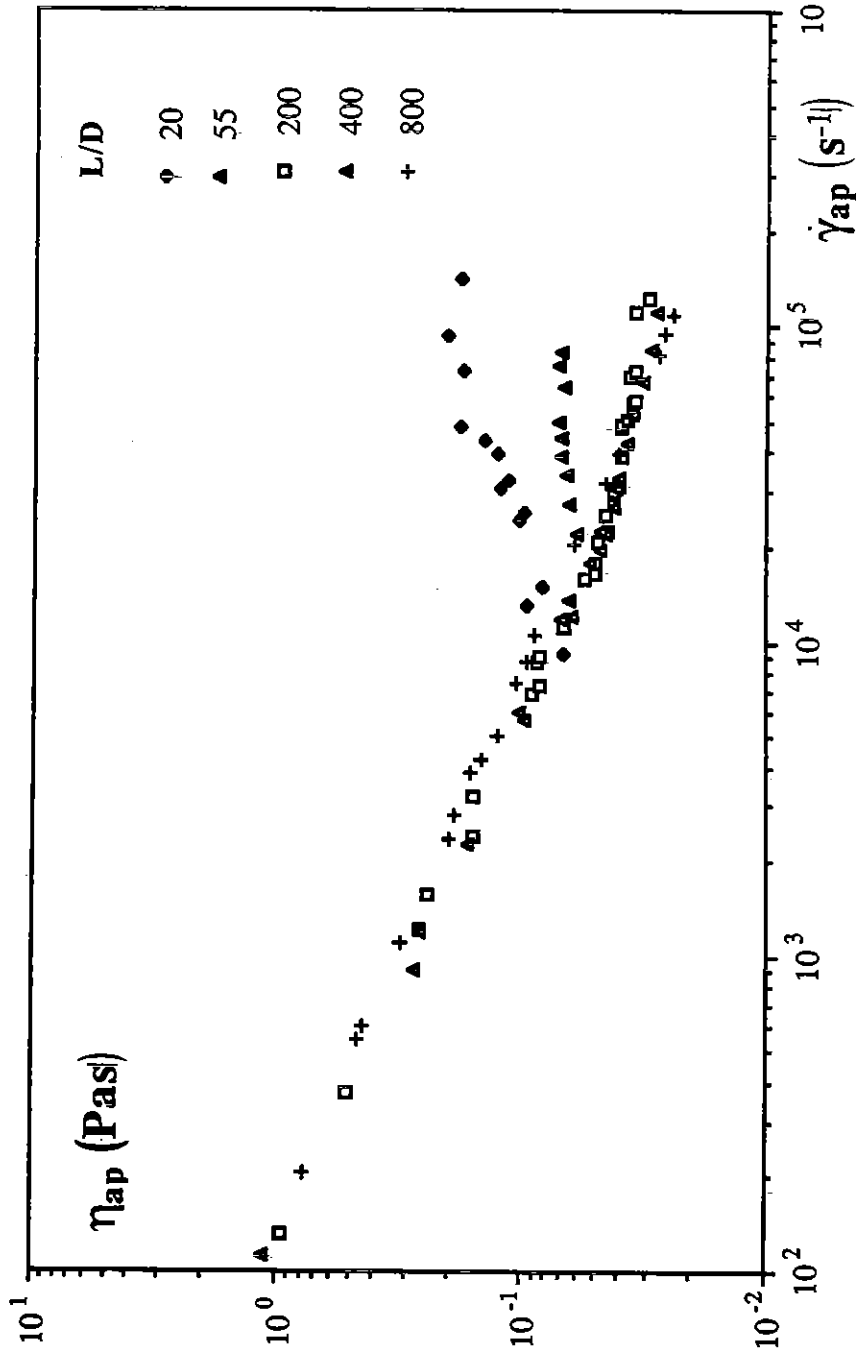

Figure 4.14 : End effect for the dies of D=1mm.

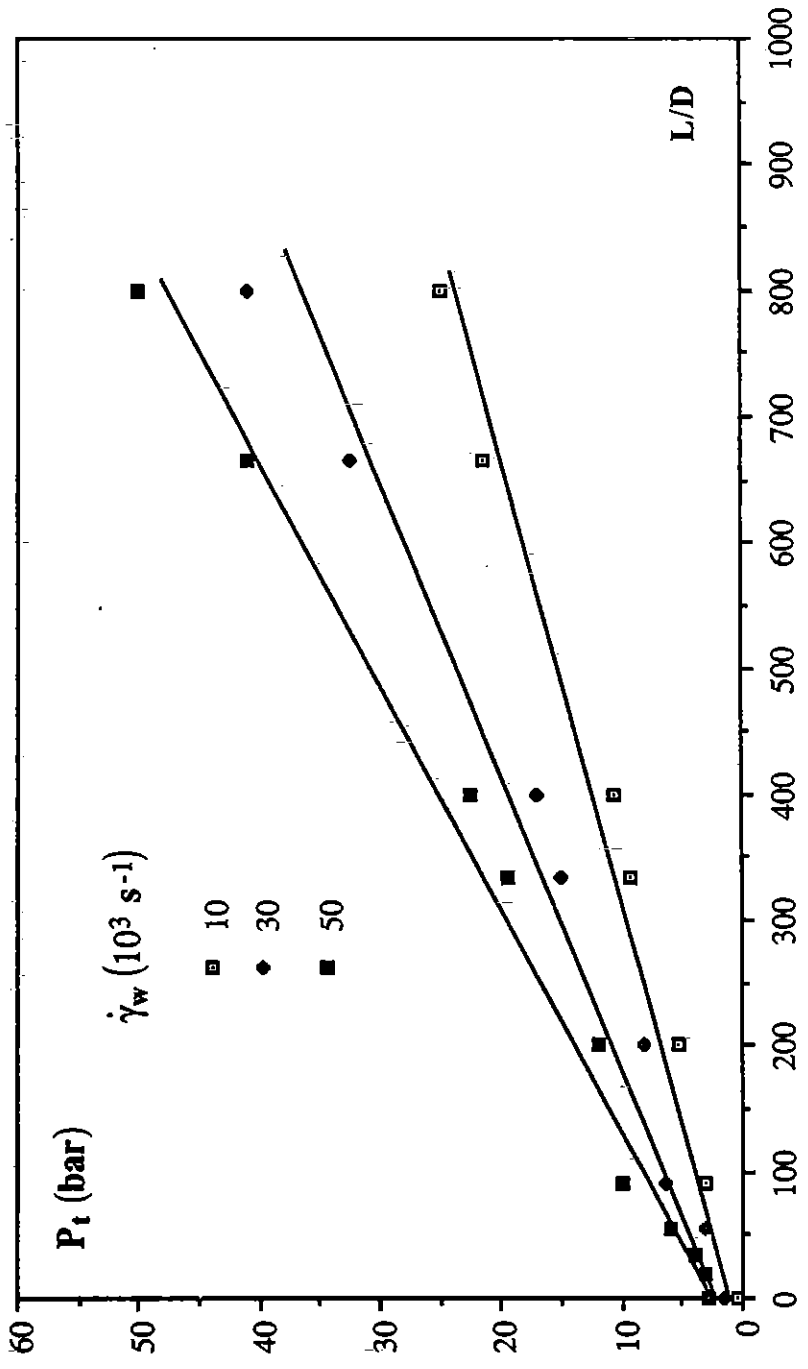

Figure 4.15 : Bagley correction for low shear rates.

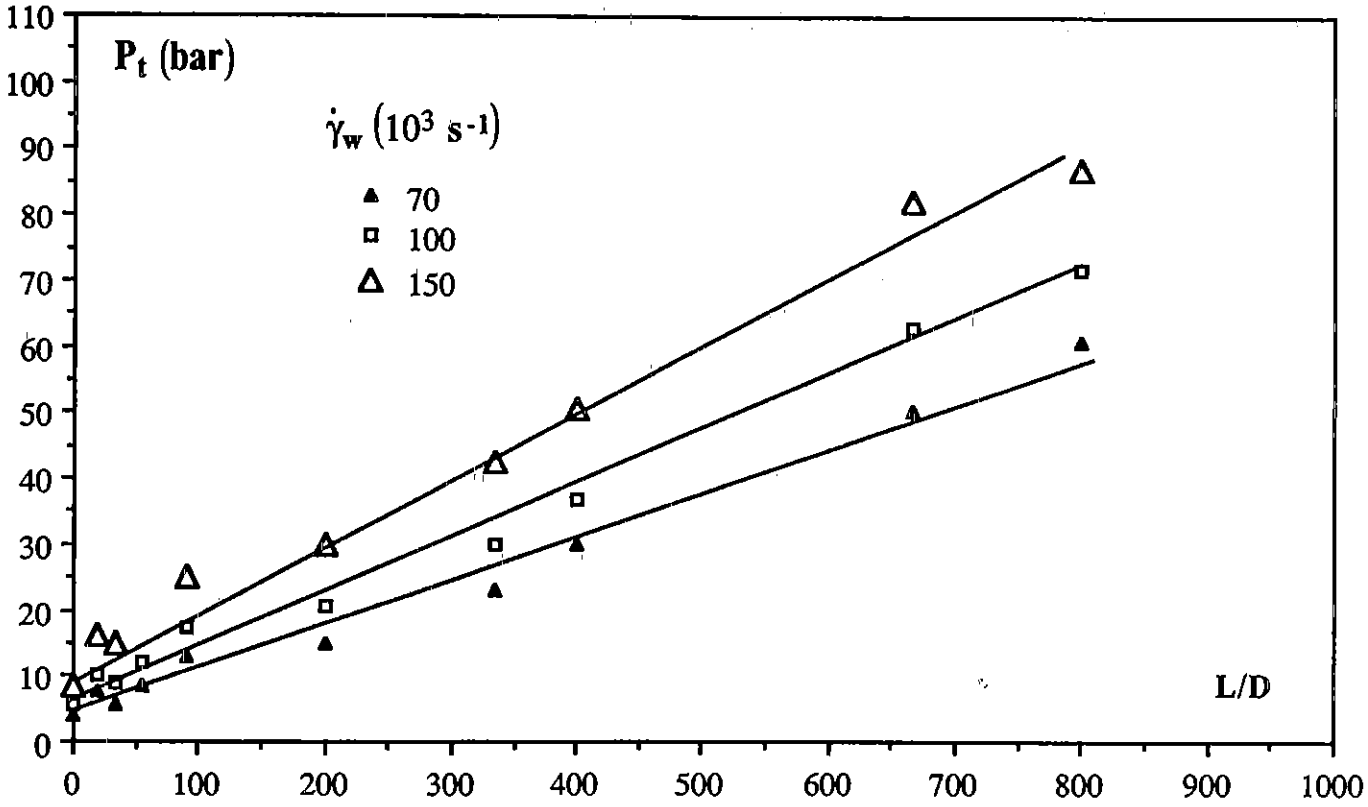

Figure 4.16 : Total pressure loss as a function of length-to-diameter ratio for high shear rates.

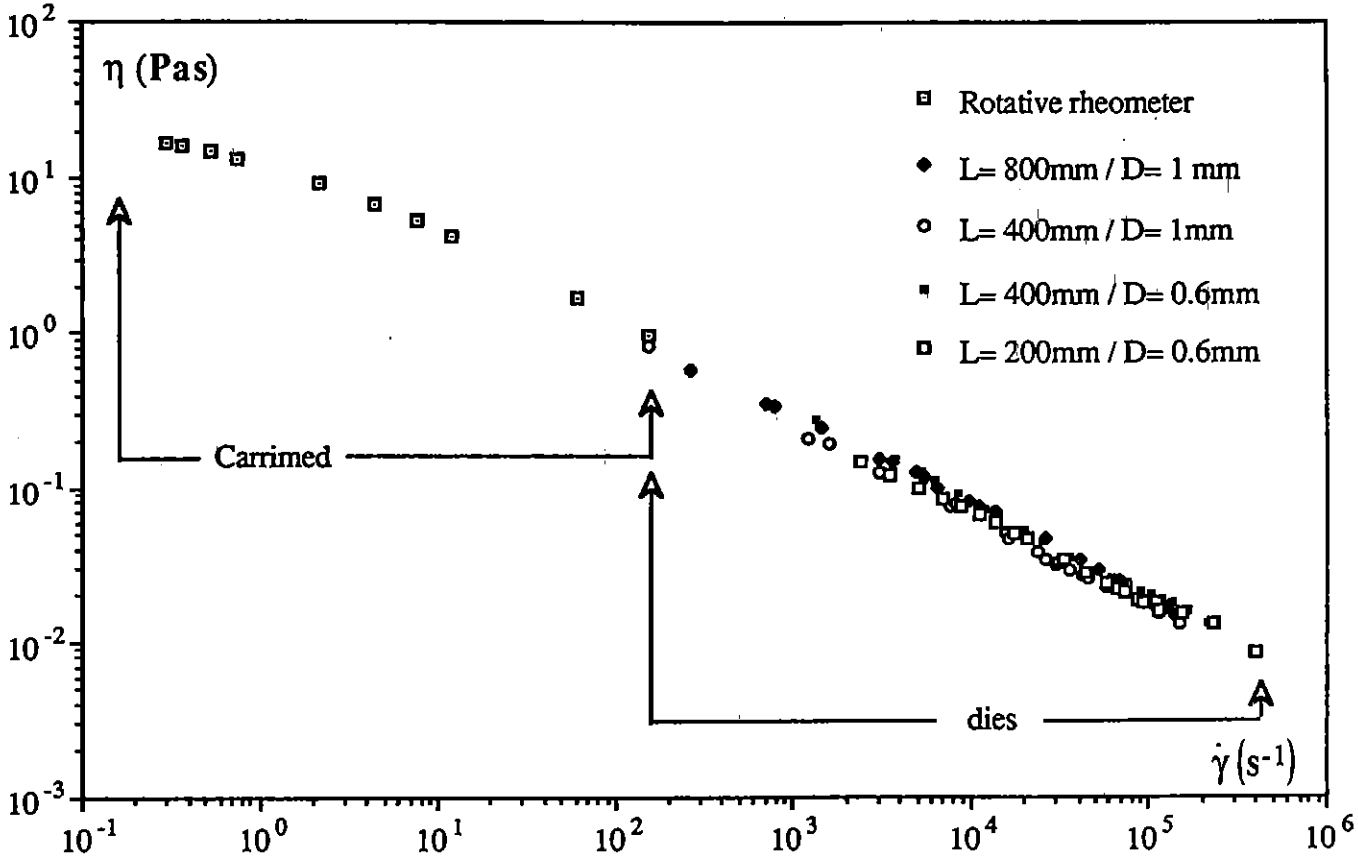

Figure 4.17 : Comparison of the shear viscosity of the PEO 4% : capillary dies and rotative rheometer.

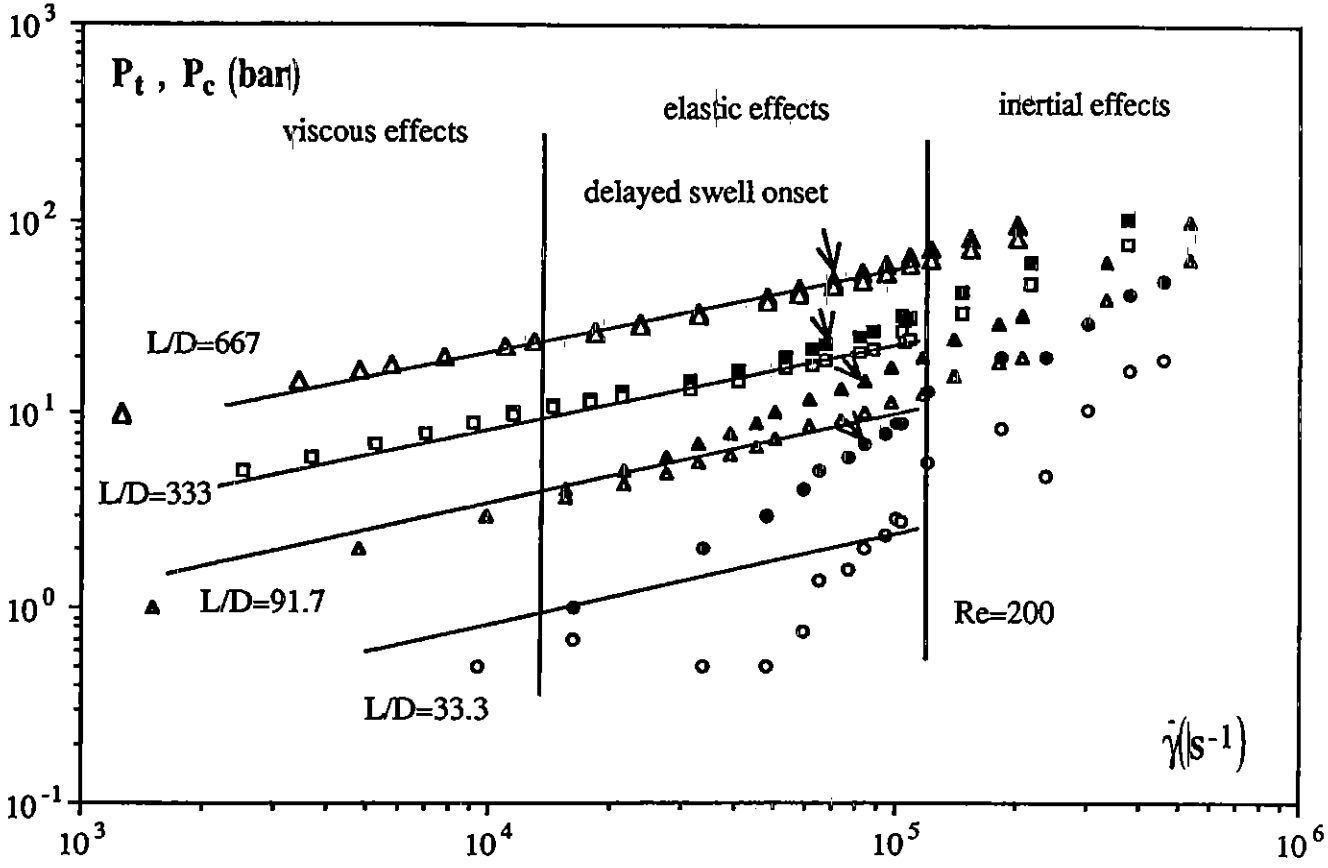

Figure 4.18 : The pressure loss corrected for the entry effects for the D=0.6mm dies.

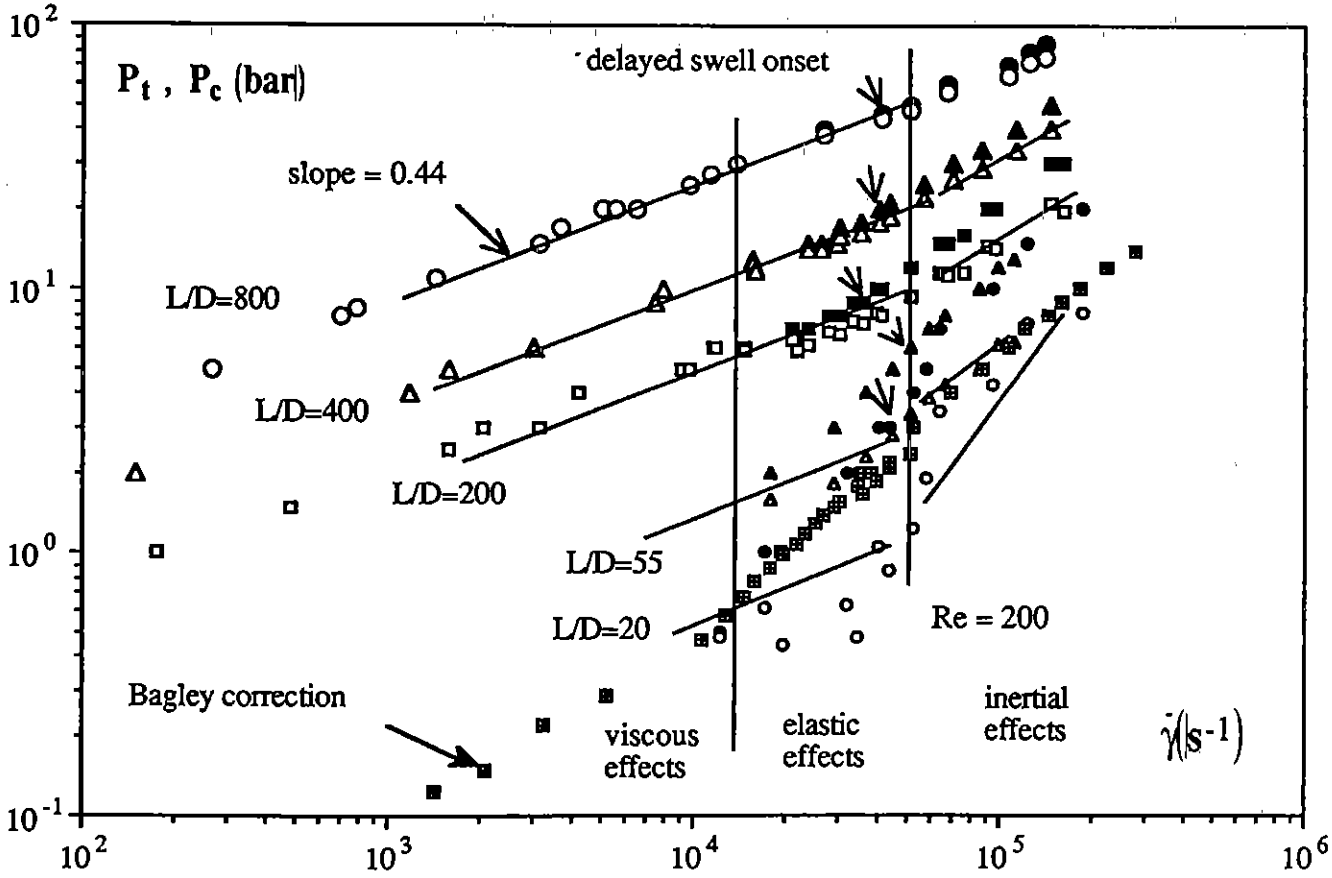

Figure 4.19 : The pressure loss corrected for the entry effects for the dies of D=1mm

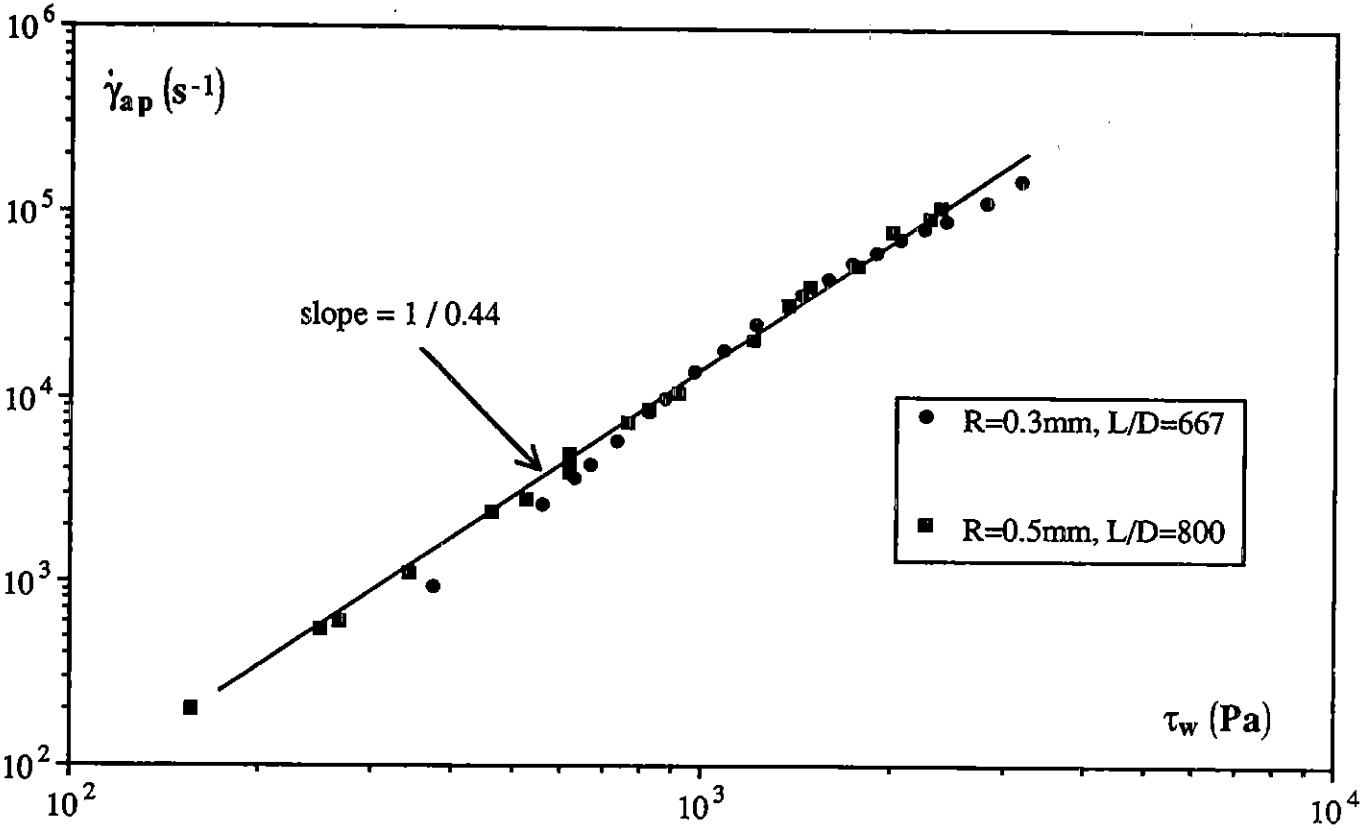

Figure 4.20 : Apparent shear rate versus the shear stress : No slip occurs

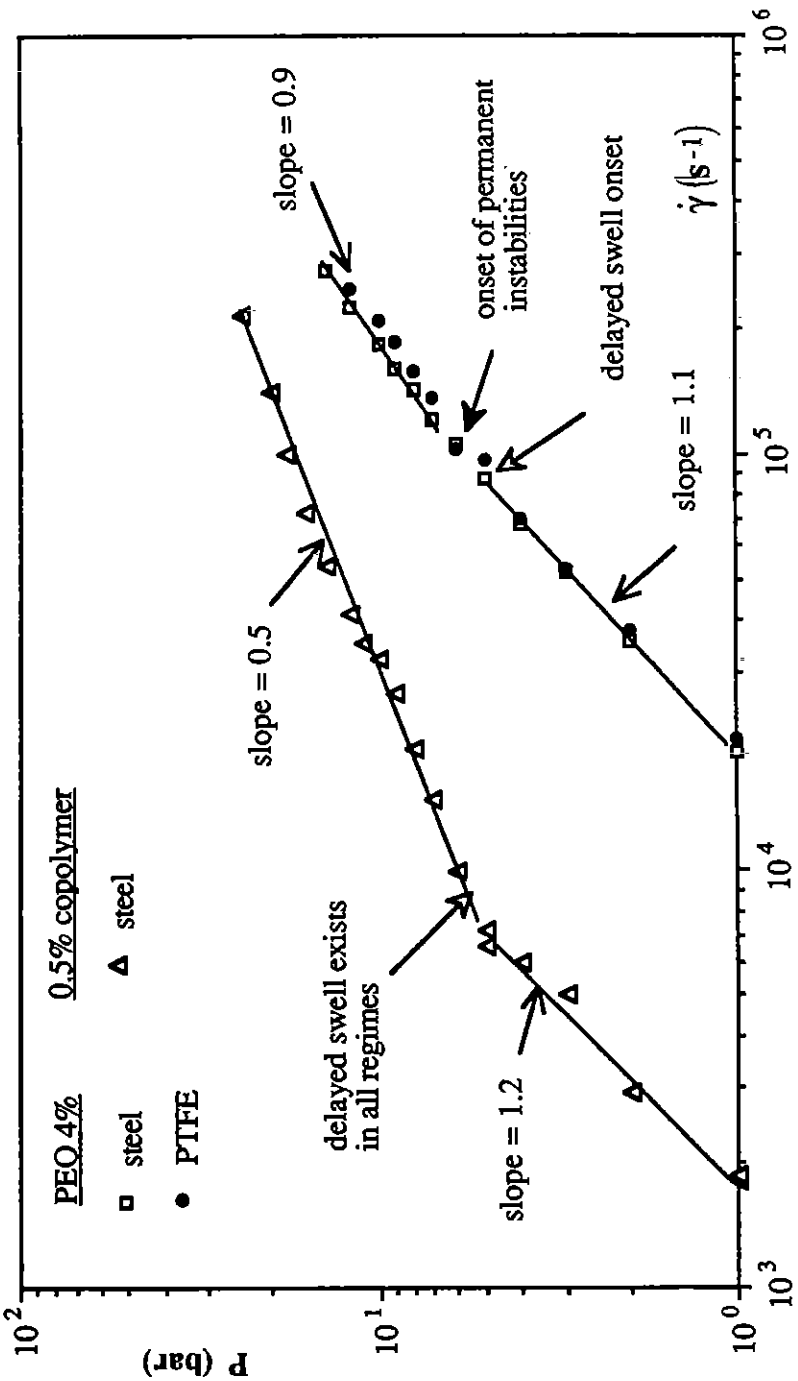

Figure 4.21 : Flow curves of the PEO 4% aqueous solution through the steel and PTFE dies and of the 0.5% copolymer solution through the steel die

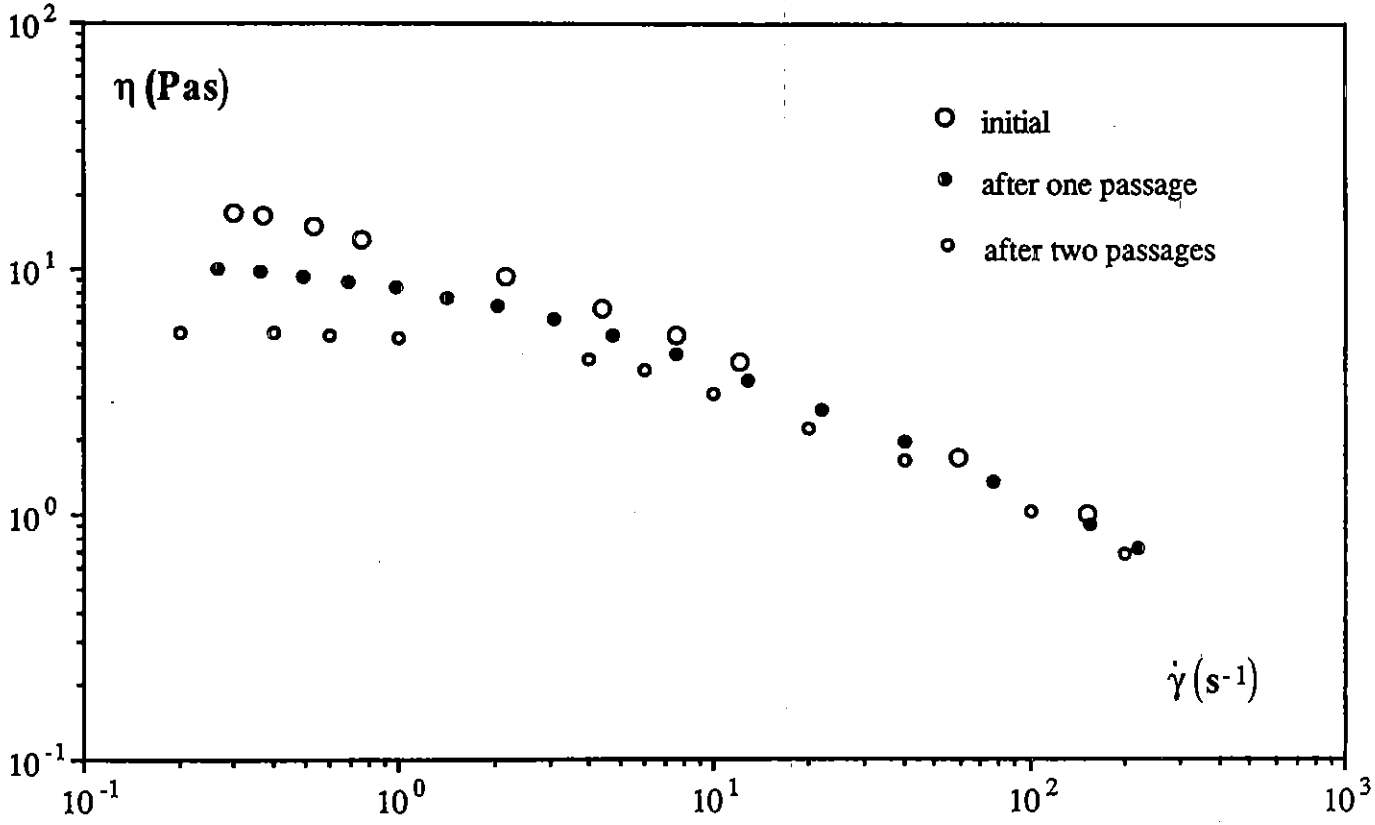

Figure 4.22 : Degradation of the aqueous PEO 4% solution

Table 4.5 : The flow curves of the 4% aqueous PEO solution through the d=1 mm dies.

L=20 mm		L=55 mm		L=200 mm		L=400 mm		L=800 mm	
$q_v\left(\frac{ml}{s}\right)$	P (bar)	$q_v\left(\frac{ml}{s}\right)$	P (bar)	$q_v\left(\frac{ml}{s}\right)$	P (bar)	$q_v\left(\frac{ml}{s}\right)$	P (bar)	$q_v\left(\frac{ml}{s}\right)$	P (bar)
0,90	0,5	0,27	0,5	0,01	1,0	0,01	2,0	0,02	5,0
1,28	1,0	0,56	1,0	0,04	1,0	0,09	4,0	0,05	8,0
1,47	1,0	1,33	2,0	0,12	2,5	0,12	5,0	0,06	8,5
2,37	2,0	2,15	3,0	0,15	3,0	0,22	6,0	0,11	11,0
2,53	2,0	2,69	4,0	0,23	3,0	0,56	9,0	0,23	15,0
3,00	3,0	3,29	5,0	0,31	4,0	0,59	10,0	0,28	17,0
3,20	3,0	3,77	6,0	0,68	5,0	1,15	13,0	0,38	20,0
3,88	4,0	4,33	7,0	0,72	5,0	1,17	12,0	0,42	20,0
3,89	4,0	4,90	8,0	0,85	6,0	1,74	15,0	0,49	20,0
4,24	5,0	6,33	10,0	0,88	6,0	1,92	15,0	0,72	25,0
4,74	7,0	7,30	12,0	1,09	6,0	2,17	16,0	0,85	27,0
7,04	10,0	8,16	13,0	1,56	7,0	2,21	17,0	1,03	30,0
9,09	15,0			1,61	6,5	2,61	18,0	2,00	40,0
13,70	20,0			1,73	7,0	3,01	20,0	3,11	46,0
				2,04	8,0	3,26	21,0	3,85	50,0
				2,22	8,0	4,17	25,0	5,10	60,0
				2,45	9,0	5,20	30,0	7,94	70,0
				2,65	9,0	6,49	33,5	9,39	80,0
				2,94	10,0	8,33	40,0	10,64	84,0
				3,08	10,0	10,87	50,0		
				3,77	12,0				
				4,71	15,0				
				4,79	15,0				
				4,97	15,0				
				5,64	16,0				
				5,66	16,0				
				6,76	20,0				
				7,09	20,0				
				10,81	30,0				
				12,05	30,0				

Table 4.6 : The flow curves of the 4% aqueous PEO solution through the d=0.6 mm dies.

L=20 mm		L=55 mm		L=200 mm		L=400 mm	
$q_v\left(\frac{ml}{s}\right)$	P (bar)	$q_v\left(\frac{ml}{s}\right)$	P (bar)	$q_v\left(\frac{ml}{s}\right)$	P (bar)	$q_v\left(\frac{ml}{s}\right)$	P (bar)
0,152	0,5	0,024	1,0	0,040	5,0	0,020	10,0
0,260	1,0	0,077	2,0	0,059	6,0	0,055	15,0
0,541	2,0	0,158	3,0	0,085	7,0	0,077	17,0
0,774	3,0	0,247	4,0	0,113	8,0	0,092	18,0
0,952	4,0	0,346	5,0	0,146	9,0	0,124	20,0
1,042	5,0	0,435	6,0	0,184	10,0	0,175	22,5
1,229	6,0	0,528	7,0	0,229	11,0	0,207	24,0
1,351	7,0	0,628	8,0	0,285	12,0	0,292	27,0
1,515	8,0	0,725	9,0	0,342	13,0	0,380	30,0
1,620	9,0	0,805	10,0	0,500	15,0	0,528	34,3
1,653	9,0	0,987	12,0	0,652	17,0	0,769	40,9
1,923	13,0	1,173	13,5	0,862	20,0	0,924	45,4
2,941	20,0	1,348	15,0	0,995	21,5	1,122	50,0
3,765	20,0	1,571	17,5	1,082	23,0	1,316	55,0
4,808	30,0	1,878	20,0	1,299	25,5	1,515	60,2
6,061	42,0	2,252	24,5	1,400	27,2	1,737	65,7
7,407	50,0	2,885	30,0	1,653	33,0	1,961	71,6
		3,279	33,0	1,685	30,5	2,432	83,0
		5,348	62,0	1,739	31,5	3,182	95,5
		8,621	100,0	2,347	43,0		
				3,472	62,0		
				6,031	102,0		